# 5
# Closed-shell Phenalenyl-based Dinuclear Iron(III) Complexes as Robust Cathode Materials for One-Compartment $H_2O_2$ Fuel Cell

***Research Article:***
(1) Kamboj, N., Dey, A., Lama, P., Majumder, M., Sengupta, S., and Metre, R. K., (2023), "Closed-shell Phenalenyl-based Dinuclear Iron(III) Complex as a Robust Cathode for One-Compartment $H_2O_2$ Fuel Cell", *Dalton Transactions*, Vol.53, pp.17163-17175.
(2) Kamboj, N., Dey, A., Birara, S., Majumder, M., Sengupta, S., and Metre, R. K., (2024), "Designing One-compartment $H_2O_2$ Fuel Cell Using Electroactive Phenalenyl-based [$Fe_2$(hnmh-PLY)$_3$] Complex as the Cathode Material", *Dalton Transactions*, Vol.53, pp. 7152-7162.

**5.1 Introduction**

The chemical science of molecules with the potential to switch between various redox electronic states on the application of external stimuli (heat, light, electric or magnetic field, etc.) has seized the interest of various state-of-the-art applications [Ahmed et al., 2018, 2022; Hicks, 2011a; Luca et al., 2013; Yang et al., 2021]. Phenalenyl (PLY), a polycyclic odd alternant hydrocarbon with the propensity to produce stable open-shell radicals, was introduced by Haddon as one of the distinctive class of organic molecules [Ahmed et al., 2021; Itkis et al., 2002]. The tricyclic π-conjugated network of highly symmetric PLY ($D_3h$) is regarded as a nano-graphene fragment [Morita et al., 2011b; Turco et al., 2023]. In the recent past, PLY as a building block has been utilized to design many new multifunctional materials with molecular bistability in various physical channels [Morita et al., 2011a; Mou et al., 2015; Pal et al., 2004; Ueda et al., 2013]. PLY exhibits a redox-amphoteric behavior through its unique NBMO (non-bonding molecular orbitals), and is known to exist in three redox states; closed-shell cation, open-shell radical, and closed-shell anion (Chart 5.1)[Kubo, 2015; Wei et al., 2017]. The gain of π-electron energy, and the delocalization energy provides stability to these three redox states. Besides, the homogenous crystal structure in such molecules allows uniform charge distribution and substantial intermolecular overlap over the entire moiety, which represses the intra-electronic repulsions in the solid state [Ahmed et al., 2022; Anamimoghadam et al., 2015; Uchida et al., 2016]. However, organic PLY radicals encountered difficulties in finding their practical applications, as they are unstable under ambient conditions, and therefore require synthetic manipulations under inert conditions [Mukherjee et al., 2017].

Mandal *et al.* have utilized the advantage of metal coordination with PLY-derived ligands to generate the stable closed-shell cationic form of PLY [Das et al., 2019c; Dey et al., 2013; Mukherjee et al., 2017; Vijaykumar et al., 2018]. With this approach, in-situ open-shell PLY radicals were generated in a series of PLY-based organoaluminium complexes, and were used to catalyze the ring-opening polymerization of ε-caprolactone and *rac*-lactide [Sen et al., 2012]. Raman *et al.* have explored the Zn(II) complex containing closed-shell PLY to fabricate a spin-memory device [Raman et al., 2013]. The PLY coordination with the first-row transition metals such as Cr(III) [Chakraborty et al., 2020b], Mn(III)/Mn(II) [Chakraborty et al., 2023; Dey et al., 2013], Fe(III) [Das et al., 2019c], Co(II) [Bellan et al., 2017; Bhunia et al., 2019b], Ni(II) [Vijaykumar et al., 2018], Cu(II) [Kamboj et al., 2022], etc; prevents the unfavorable oxidation states on central metal ions during the homogeneous catalytic cycles.

PLY possesses adequate potential to function as an "electron reservoir" that, upon coordination with a transition metal ion, may lead to molecules with superior redox

properties. The fundamental PLY moiety, *9-hydroxy-1H-phenalen-1-one,* which is often identified with the common name PLY itself, is the key precursor to synthesize PLY-based ligands (Chart 5.2) [Ahmed et al., 2022]. Since the well-developed π-conjugated network of *9-hydroxy-1H-phenalen-1-one* contains a very strong intra-molecular H-bonding interaction, the nucleophilic substitution or addition on 1- or 9- position is challenging. The most convenient approach by Franz *et al.* [Ahmed et al., 2022; Franz, 1979; Franz et al., 1978] has devised a synthetic pathway to conveniently disrupt the hydrogen bond using silver oxide and alkyl iodide to give *9-alkoxy-1H-phenalen-1-one*, as shown in Chart 5.2. Such β-keto ether functionalities can undergo nucleophilic substitution reactions with secondary or primary amines to give PLY-based ligands with greater potential for back-bonding in metal complexes. Despite the introduction of strong coordinating sites, this synthetic protocol is often challenged by longer reaction times [Banik et al., 2018; Chakraborty et al., 2020b; Dale et al., 2019]. Although this generalized synthetic approach has been used to functionalize PLY-based ligands for the last two decades, it resulted invariably in the formation of mononuclear metal complexes so far.

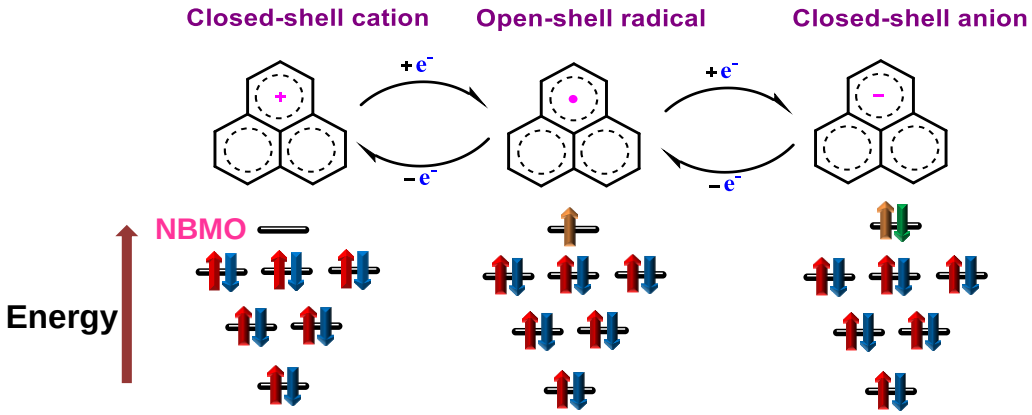



**Chart 5.1** General representation of the Hückel molecular orbitals and energy levels for the un-substituted phenalenyl molecules [Mukherjee et al., 2017].

Our group has recently gained interest in robust PLY-based systems and has reported the first Cu(II)-PLY complex and explored the catalytic behavior for the oxidation of polycyclic aromatic hydrocarbons(PAHs) [Kamboj et al., 2022]. Furthermore, we have utilized a Co(II) complex with a closed-shell cationic state of PLY to construct a resistive memory device [Kamboj et al., 2023a]. As a part of our continued interest in exploring PLY-based metal complexes, we herein report a new PLY precursor moiety, *9-hydrazineyl-1H-phenalen-1-one* (Hz-PLY), which is further functionalized to design the PLY-based Schiff base ligands, *(E)-9-(2-(2-hydroxy-3-methoxybenzylidene)hydrazineyl)-1H-phenalen-1-one* (hmbh-PLY$H_2$) and *(E)-9-(2-((2-hydroxynaphthalen-1-yl)methylene)hydrazineyl)-1H-phenalen-1-one* (hnmh-PLY$H_2$). Utilizing this approach, we have introduced PLY moiety to the class of Schiff base ligands in this report. Consequently, using our ligand design (with flexible N-N bond), we hypothesized a scope for the formation of muti-nuclear metal complexes containing PLY units. To realize such a proposal, herein, we have reacted the newly synthesized hmbh-PLY$H_2$ and hnmh-PLY$H_2$ ligands with $FeCl_3$, to obtain the first PLY-functionalized dinuclear iron(III) complexes, [$Fe^{III}_2$(hmbh-PLY)$_3$], **3**, and [$Fe^{III}_2$(hnmh-PLY)$_3$], **4**. Interestingly, both the complexes undergoes up to five electron reductions, under an applied cathodic sweep.

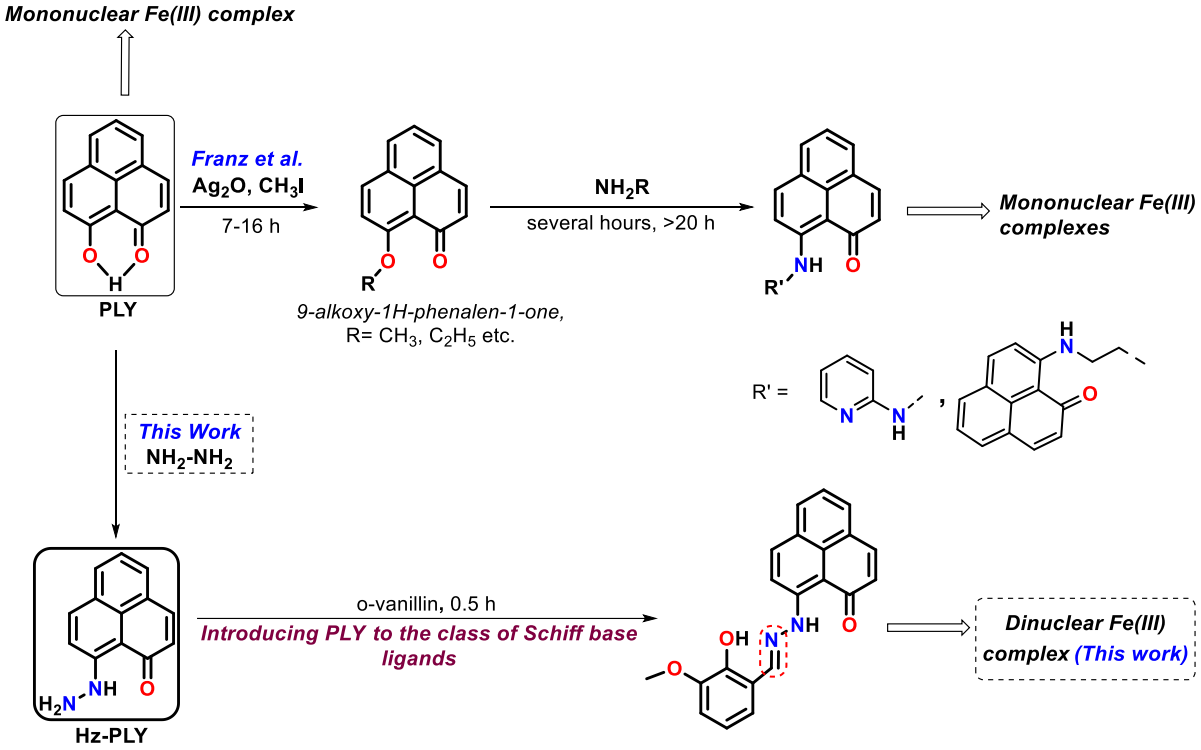



**Chart 5.2** Schemes depicting functionalization on the 9-position of the 9-hydroxy-1H-phenalen-1-one (PLY) and corresponding Fe(III) complexes obtained.

On the other hand, such redox-interesting Fe-based cathodes are known to substantially decrease the overpotential required for $H_2O_2$ reduction in a one-compartment $H_2O_2$ fuel cell [Sun et al., 2022b; Yamada et al., 2011; Yang et al., 2018a, 2019]. $H_2O_2$ is a potential next-generation energy carrier as its output potential is theoretically analyzed to be 1.09 V, which is in close proximity to the output potentials of well-known hydrogen (1.23 V), and direct methanol fuel cells (1.21 V) [Wang et al., 2022; Yamada et al., 2015]. Therefore, due to the observed redox-interesting behavior of complexes **3** and **4,** we have employed the as-synthesized dinuclear Fe(III) complexes as pilot cathode materials for a membrane-less one-compartment $H_2O_2$ fuel cell. The considerable low overpotential for the reduction of $H_2O_2$ over the Fe(III) metal center resulted in peak power densities (PPD) of 2.41 mW $cm^2$ for complex **3** and 2.84 mW $cm^{-2}$ for complex **4**, which are the highest amongst all molecular complexes reported so far in the literature. The mechanism for $H_2O_2$ reduction by these dinuclear complexes is elucidated by corroborating the electrochemical and density functional theory (DFT) studies. Further, comparative experimental and DFT studies have been employed to discuss the ligand substitution's effect on the observed PPD.

## 5.2 Experimental Section

### 5.2.1 Synthesis of the ligands

***9-hydrazineyl-1H-phenalen-1-one* (Hz-PLY):** *9-hydroxy-1H-phenalen-1-one* (500.0 mg, 2.5 mmol) was added to hydrazine hydrate (10 ml), and the resultant solution was heated for 8 hours at 140 °C. The reaction progress was continuously monitored over TLC. After the completion of the reaction, the resultant orange precipitate was filtered and washed multiple times with water, which on recrystallization from methanol gave pure Hz-PLY: Yield: 510 mg (95 %). $^1$H NMR (500 MHz, $CDCl_3$, $Me_4Si$) δ (ppm): δ 12.9 (s, 1H), 7.9 (dd, 2H, *J* = 26.3, 9.4 Hz), 7.8 (t, 3H, *J* = 8.3 Hz), 7.4 (t, 1H, *J* = 7.6 Hz), 7.2 (s, 1H, $CDCl_3$), 7.0 (d,

1H, *J* = 9.4 Hz), 4.0 (s, 2H). $^{13}$C NMR (125 MHz, $CDCl_3$, $Me_4Si$): δ 183.3, 158.2, 138.1, 138.1, 131.5, 131.2, 128.2, 128.0, 125.2, 124.7, 121.9, 114.4, 107.1, 77.3 ($CDCl_3$). FT-IR (KBr pellets, ν/cm$^{-1}$): 3300(m), 3028 (w), 1633(s), 1572(s), 1110(s). HRMS ($CH_3CN$, positive ionization): calcd. for $C_{13}H_{10}N_2O$ m/z = 211.0866 $[M+H]^+$, found 211.0867 $[M+H]^+$.

***9-(2-(2-hydroxy-3-methoxybenzylidene) hydrazineyl)-1H-phenalen-1-one,* hmbh-PLY$H_2$:** To a suspension of Hz-PLY (400.0 mg, 1.9 mmol) and o-vanillin (289.0 mg, 1.9 mmol) in methanol, a catalytic amount of conc. HCl (2-3 drops) was added. The mixture was stirred under reflux for 1 hour. On completion of the reaction, the product was isolated in the form of a dark red precipitate. Analytically pure crystals of hmbh-PLY$H_2$ were obtained from acetonitrile solution at room temperature. Yield: 590 mg (90 %). $^1$H NMR (500 MHz, $CDCl_3$, $Me_4Si$) δ (ppm): δ 15.1 (s, 1H), 10.9 (s, 1H), 8.3 (s, 1H), 8.0 (d, *J* = 9.3 Hz, 1H), 7.9 (d, *J* = 7.8 Hz, 1H), 7.8 (dd, *J* = 8.1, 4.3 Hz, 2H), 7.8 (d, *J* = 9.3 Hz, 1H), 7.5 (t, *J* = 7.6 Hz, 1H), 7.2 (s, 1H, $CDCl_3$), 6.9 (d, *J* = 9.4 Hz, 1H), 6.92 – 6.89 (m, 2H), 6.9 – 6.8 (m, 1H), 3.9 (s, 3H). $^{13}$C NMR (125 MHz, DMSO-d6, $Me_4Si$) δ (ppm): δ 183.6, 151.4, 148.2, 146.4, 145.4, 139.4, 138.7, 132.5, 132.1, 127.7, 125.1, 123.1, 118.5, 115.0, 113.6, 106.4, 55.9, 39.5 (DMSO-$d_6$). FT-IR (KBr pellets, ν/cm$^{-1}$): 3662(s), 3118(m), 1633(s), 1579(s), 1514(s), 1255(s). HRMS ($CH_3CN$, positive ionization): calcd. for $C_{21}H_{16}N_2O_3$ m/z = 345.1234 $[M+H]^+$, found 345.1242 $[M+H]^+$.

***(E)-9-(2-((2-hydroxynaphthalen-1-yl)methylene)hydrazineyl)-1H-phenalen-1-one*, hnmh-PLY$H_2$**: Hz-PLY (1 mmol, 0.21 g) and *2-hydroxy-1-naphthaldehyde* (1mmol, 0.17 g) were simultaneously added to 50 ml methanol. The reaction mixture was refluxed for 1 hour to yield a red precipitate. The precipitate was subsequently washed with cold methanol. Recrystallization from acetonitrile solution resulted in bright red X-ray quality needle-like crystals. Yield: 0.34 g (92%). $^1$H NMR (500 MHz, $CDCl_3$, $Me_4Si$) δ (ppm): 15.36 (s, 1H), 12.1 (s, 1H), 9.2 (s, 1H), 8.0 (d, *J* = 9.2 Hz, 2H), 7.9 (d, *J* = 7.7 Hz, 1H), 7.8 (d, *J* = 7.7 Hz, 2H), 7.7 (dd, *J* = 11.6, 9.1 Hz, 2H), 7.7 (d, *J* = 8.0 Hz, 1H), 7.5 (t, *J* = 7.7 Hz, 1H), 7.4 (t, *J* = 7.6 Hz, 1H), 7.3 (t, *J* = 7.4 Hz, 1H), 7.00 (d, *J* = 9.4 Hz, 1H). $^{13}$C NMR (126 MHz, $CDCl_3$) δ (ppm): 183.7, 158.5, 151.3, 147.1, 139.2, 138.7, 133.4, 132.4, 131.9, 131.8, 129.2, 128.3, 127.8, 127.8, 127.7, 125.8, 125.7, 123.8, 123.1, 120.1, 118.8, 114.4, 108.6, 107.6. FT-IR (KBr pellets, ν/cm$^{-1}$): 3668(m), 3223(m), 1621(s), 1577(s), 1511(s), 1258(s). HRMS ($CH_3CN$, positive ionization): calcd. for $C_{24}H_{17}N_2O_2$ m/z = 365.1290 $[M+H]^+$, found 365.1286 $[M+H]^+$.

### 5.2.2 Synthesis of complexes

**[$Fe^{III}_2$(hmbh-PLY)$_3$], 3**

For the synthesis of complex 3, anhy. $FeCl_3$ (32.4 mg, 0.2 mmol) dissolved in 5 ml methanol was added to a 10 mL methanolic solution of hmbh-PLY$H_2$ (103.5 mg, 0.3 mmol), and trimethylamine (100 μL). The mixture was stirred under reflux for 24 h, leading to the formation of a black precipitate. Recrystallization of the precipitate from $CHCl_3$ yielded complex 3 in good yield. X-ray quality crystals were obtained from the slow diffusion of hexane to the saturated solution of complex 3 in $CHCl_3$. Yield (based on Fe): 75 mg (66 %). Elemental analysis: calcd. for $C_{63}H_{42}Fe_2N_6O_9$: C, 66.45; H, 3.72; N, 7.38. Found: C, 66.29; H, 4.06; N, 7.23. FT-IR (KBr pellets, ν/cm$^{-1}$): 3136(m), 1583(s), 1490(s), 1446(s), 1326(s), 1261(s), 462(w). UV-vis [DCM, λ/nm (ε in M$^{-1}$ cm$^{-1}$)]: 566(18950), 463(27272), 349 (51168), 294(61689). HRMS ($CH_3CN$, positive ionization): calcd. for $C_{63}H_{42}Fe_2N_6O_9$ m/z = 1139.1785 $[M+H]^+$, found 1139.1787 $[M+H]^+$.

**[$Fe_2$(hnmh-PLY)$_3$], 4:** To a methanolic suspension containing hnmh-PLY$H_2$ (0.3 mmol, 109.2 mg) and 100 μL triethylamine (excess), anhydrous $FeCl_3$ (0.2 mmol, 32.4 mg) was added and the reaction mixture was set up to reflux under inert atmosphere for 24 hours. The reaction mixture

turned black during the reaction, and the black precipitate was isolated, and thoroughly washed with methanol. Recrystallization of the as-obtained precipitate from the $CHCl_3/CH_3CN$ (1:1) solvent mixture yielded complex **4** in the form of black needles which were suitable for SCXRD analysis. Yield (based on Fe): 87.46 (73%). Elemental analysis: calcd. for $C_{72}H_{42}Fe_2N_6O_6$: C, 72.13; H, 3.53; N, 7.01. Found: C, 71.45; H, 3.68; N, 6.81. FT-IR (KBr pellets, $\nu/cm^{-1}$): 3170(m), 1583(s), 1533(s), 1344(s), 1191(m), 486(w). UV-vis (DCM, $\lambda$/nm ($\varepsilon$ in $M^{-1}cm^{-1}$)): 575(18950), 385(27272), 322 (51168), 292(61689). HRMS ($CH_3CN$, positive ionization): calcd. for $C_{72}H_{42}Fe_2N_6O_6$ m/z = 1198.1943 $[M+H]^+$, found 1199.1984 $[M+H]^+$.

### 5.2.3 Preparation of Electrode for $H_2O_2$ Reduction

The bare glassy carbon (GC) electrode (circular surface area = 0.07 $cm^2$) was polished successively with 1.0, 0.3, and 0.05 µm alumina until a mirror surface was formed. To eliminate any remaining alumina particles stuck on the electrode's surface, the electrode was ultrasonically cleaned twice, first in distilled water and then in ethanol [McCreery, 2008]. Nickel foam was treated with dilute HCl (10%) in an ultrasonic bath for 5 minutes to remove the surface oxide layer. Further, thorough rinsing with deionized water and absolute ethanol was followed before the fuel cell experiments. Complex **3** (3.0 mg, 2.6 mmol) was dissolved in 1 ml DMF. 10.0 µl of this solution was drop cast on a GC electrode, followed by 3.0 µL Nafion solution (5 wt. %), and dried to give **GC-**3 electrode. Complex **4** (**GC-4**), $FeCl_3$, and ligand-modified GC electrodes were prepared similarly. The sample for the carbon black mixed electrode (**GC-3C** and **GC-4C** ) was prepared by finely grinding 10% (wt/wt) carbon black with the respective complexes in a motor pastle with N-methyl pyrrolidine (NMP) solvent. The uniformly mixed slurry (10.0 µL) was drop cast on a GC electrode, followed by 3.0 µL Nafion solution (5 wt. %), and dried. All the measurements were repeated at least 5 times to ensure the reproducibility of the performance tests.

### 5.2.4 Computational Details

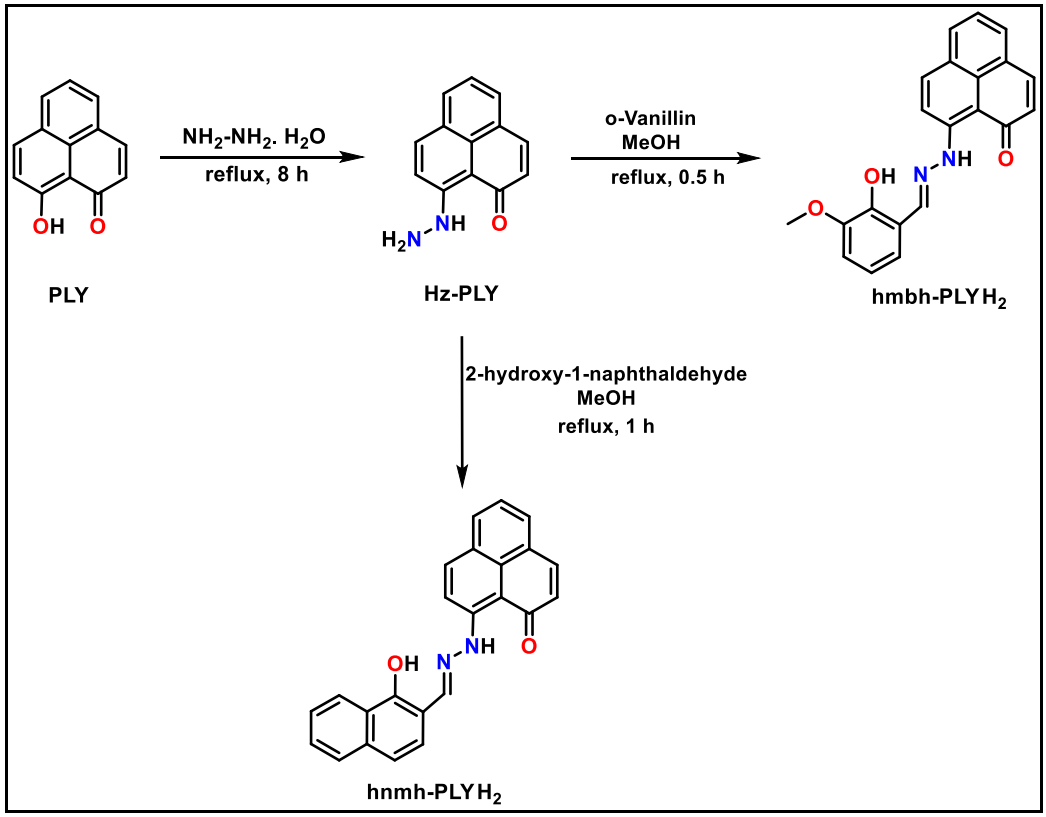
The Density Functional Theory (DFT) computations were performed using the ORCA 5.0.2 programs [Neese et al., 2020b]. The geometry of complexes was optimized by using a hybrid functional B3LYP method in conjugation with a basis set def2-SVPon ligands (C, H, O, N) and a basis-set def2-TZVP on iron centers [Weigend et al., 2005b]. To improve the computational speed, the RIJCOSX approximation [Kollmar et al., 2019a] with a combination of an auxiliary basis set (def2/J)[Weigend, 2006b] was also employed in all spin-unrestricted DFT calculations. No symmetry restrictions (i.e. C1) were held during the geometry optimizations. Frequency analysis calculations were performed to verify the minimum character of all optimized structures (no imaginary frequency) and transition state structures with one imaginary frequency. The resultant geometries from optimization were used in subsequent single-point energy calculations at the B3LYP/def2-TZVP+def2-TZVPP method (metal centers and its coordination environment are treated with def2-TZVPP basis function) along with Grimme's dispersion correction, D3BJ [Allouche, 2011; Grimme et al., 2010a]. The Natural Population Analysis (NPA) and Natural Bond Order (NBO) analysis were performed at the same level of theory (B3LYP+D3BJ/def2-TZVP+def2-TZVPP). The NBO 7.0. [NBO 7.0. Glendening, E. D.; Badenhoop, J. K.; Reed, A. E.; Carpenter, J. E.; Bohmann, J.; Morales, C. M.; Karafiloglou, P.; Landis, C. R.; and Weinhold, F. Theoretical Chemistry Institute, University of Wisconsin, Madison, n.d.] Program interfaced with ORCA 5.0.2 program was used for the present study. The solvent effect in redox calculations was considered by using the CPCM method [Barone et al., 1998b] with DMF. VMD [Humphrey et al., 1996] software was used for the visualization of molecular orbitals and

spin density. The mechanistic investigation of $H_2O_2$ reduction by a Fe-based electrocatalyst is carried out at the B3LYP+D3BJ/def2-SVP+def2-TZVP (the metal ions are only treated with triple zeta basis function) level of theory. A few preliminary calculations are carried out using the semiempirical tight-binding method GFN2-xTB via the Orca/XTB 6.4.0 interface [Bannwarth et al., 2019, 2021].

## 5.3 Results and Discussion

### 5.3.1 Synthetic Aspects

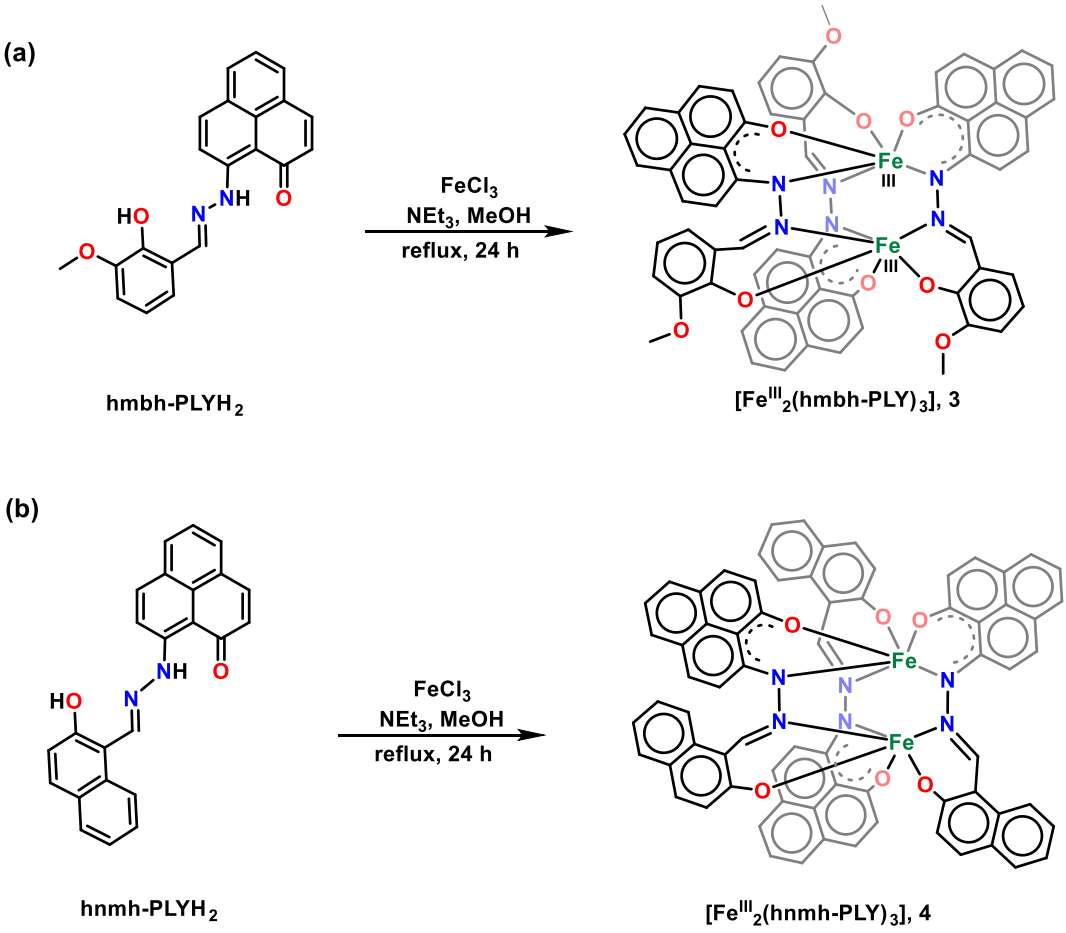
The ligand *(E)-9-(2-(2-hydroxy-3-methoxybenzylidene)hydrazineyl)-1H-phenalen-1-one, hmbh-PLYH₂* and *(E)-9-(2-((2-hydroxynaphthalen-1-yl)methylene)hydrazineyl)-1H-phenalen-1-one, hnmh-PLYH₂* were prepared via multiple-step conversions as depicted in Scheme 5.1. *9-hydroxy-1H-phenalen-1-one* on the treatment with hydrazine hydrate under the reflux conditions resulted in the formation of *9-hydrazineyl-1H-phenalen-1-one,* Hz-PLY. The reactive primary amine of the Hz-PLY undergoes a Schiff base reaction with the *4-hydroxy-3-methoxybenzaldehyde* (o-vanillin) and *2-hydroxy-1-naphthaldehyde* in hot methanol to yield the respective hmbh-PLYH₂ and hnmh-PLYH₂ ligands. The successive rearrangement of the electron distribution on the phenalenyl ring during these two chemical modifications is apparent from the chemical shifts observed in the $^1$H NMR spectra (appendix section 5.6). Both the hmbh-PLYH₂ and hnmh-PLYH₂ ligands existed in one of the tautomeric forms around the 1- and 9-position of the phenalenyl ring and the N-H resonance for these ligands is observed at δ 15.1 ppm and 15.3 ppm, respectively (appendix section 5.6). The structure of the designed ligands was further confirmed using the single-crystal X-ray diffraction (SCXRD) technique (Figure 5.1). Details of crystallographic parameters are given in Tables 5.1 and 5.2.



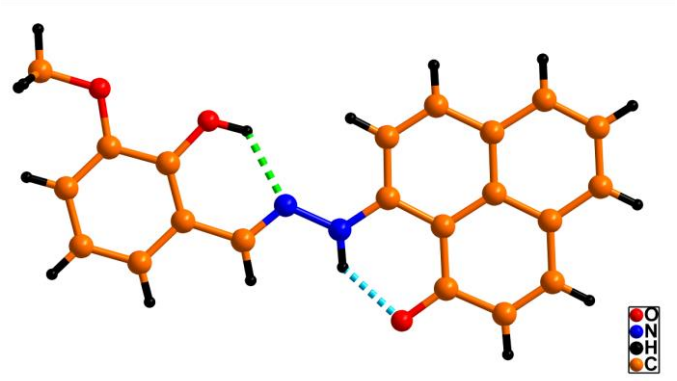

**Scheme 5.1** Synthesis of hmbh-PLYH₂ and hnmh-PLYH₂ ligands.

The reaction of hmbh-PLYH₂ with anhyd. $FeCl_3$ in 3:2 molar ratios, in the presence of $NEt_3$ base in methanol, yielded a black precipitate (Scheme 5.2). The precipitate was

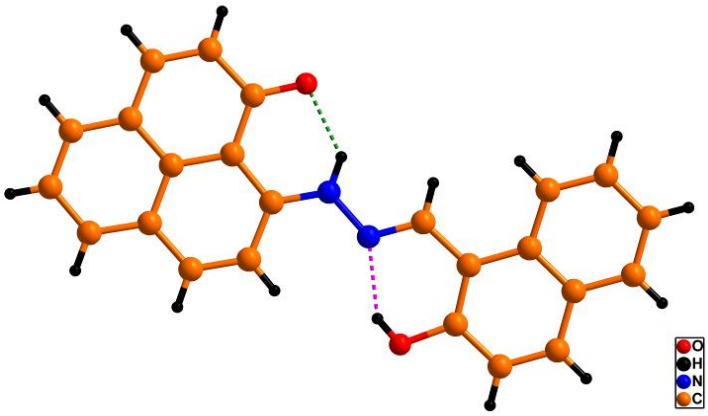
dissolved in $CHCl_3$ solvent, which on slow evaporation resulted in single crystals of **3**. The molecular structure of the complex $[Fe^{III}_2(hmbh\text{-}PLY)_3]$, **3** was confirmed by the SCXRD technique (Figure 5.1). Similarly, complex **4** was synthesized from the hnmh-$PLYH_2$ ligand and structurally characterized by the SCXRD technique. Details of crystallographic parameters are given in Tables 5.1 and 5.2. Complexes **3** and **4** consist of two hexa-coordinated Fe(III) metal ions, surrounded by the N3O3 coordination sphere. For both the complexes, the two Fe(III) centers adopt distinct coordination types, where Fe1 is coordinated directly to one PLY unit, and Fe2 is coordinated with the other two PLY units. The spatial distance between two Fe(III) centers, Fe1---Fe2 is measured as 3.811(1) Å and 3.797(7) Å for complexes **3** and **4**, respectively. For the steric requirements, the ligand moieties are twisted along the N-N bonds to afford the "$\mu$-N-N" bridge that connects the two Fe(III) centers. The bond lengths corresponding to the three $\mu$-N-N bridges in complex **3** are; [$\mu$-N1-N2, 1.428(6) Å; $\mu$-N3-N4, 1.431(6) Å; $\mu$-N5-N6, 1.416(6) Å]. Three such $\mu$-N-N bridges are also present in complex **4**, and their corresponding bond lengths are; [$\mu$-N1-N2, 1.424(30); $\mu$-N3-N4, 1.428(40) Å; $\mu$-N5-N6, 1.413(37) Å].



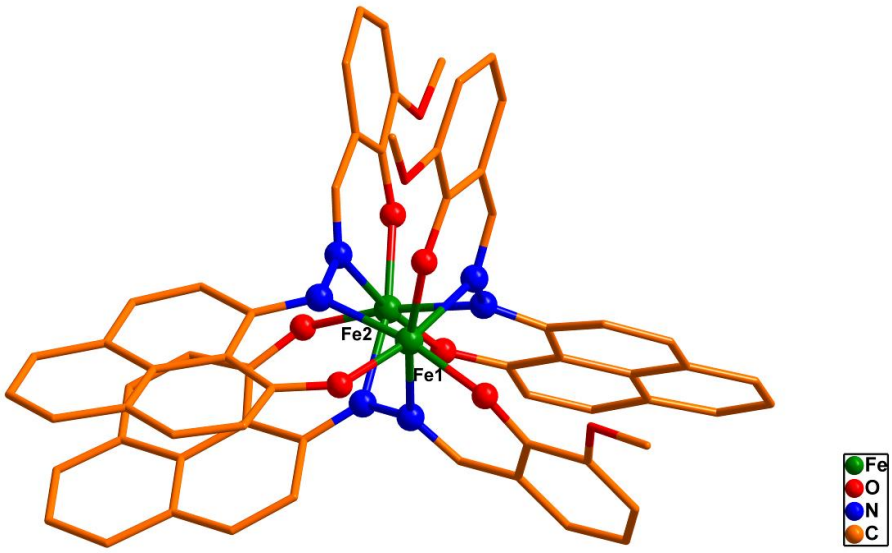

**Scheme 5.2** Synthesis of complexes, **(a) 3** and **(b) 4**.




(a)




(b)




(c)

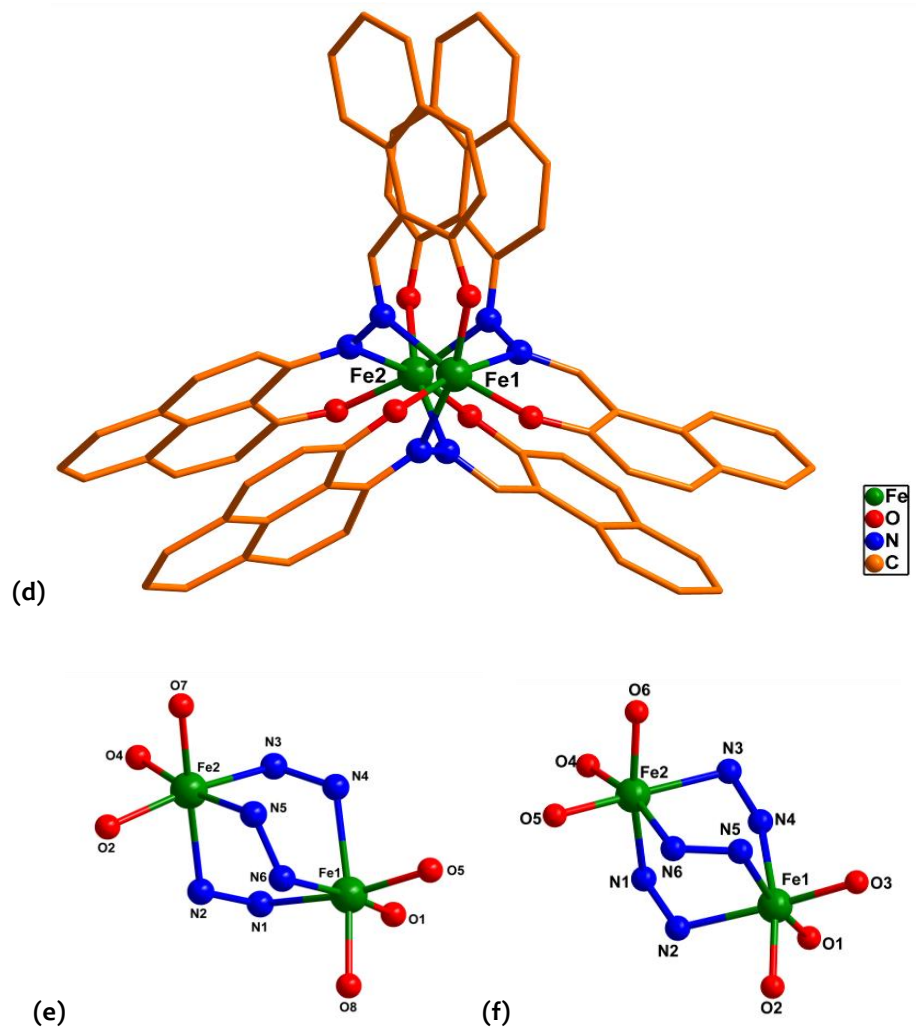



**Figure 5.1** Molecular structure of **(a)** hmbh-PLYH$_2$, **(b)** hnmh-PLYH$_2$, **(c)** complex **3**, and **(d) 4** (hydrogen atoms are omitted for clarity). **(e)** The coordination environment of the two Fe(III) centers in complexes, **(e) 3** and **(f) 4**.

**Table 5.1** Crystal data and structure refinement parameters for the ligand, hmbh-PLYH$_2$ and [Fe$^{III}_2$(hmbh-PLY)$_3$], complex **3** (CCDC 2283565, 2283566)

| Identification code | hmbh-PLYH$_2$ | [Fe$^{III}_2$(hmbh-PLY)$_3$], **3** |
|---|---|---|
| Empirical formula | $C_{21}H_{16}N_2O_3$ | $C_{65}H_{44}N_6O_9Cl_6Fe_2$ |
| Formula weight | 344.36 | 1377.46 |
| Temperature/K | 100 | 100 |
| Crystal system | orthorhombic | monoclinic |
| Space group | *Aba2* | $P2_1/c$ |
| a/Å | 16.38(2) | 23.2460(12) |
| b/Å | 29.87(4) | 13.2054(7) |
| c/Å | 6.843(9) | 19.6226(10) |
| α/° | 90 | 90 |
| β/° | 90 | 101.358(2) |
| γ/° | 90 | 90 |
| Volume/Å$^3$ | 3348(7) | 5905.6(5) |
| Z | 8 | 4 |
| $\rho_{calc}$g/cm$^3$ | 1.366 | 1.549 |
| μ/mm$^{-1}$ | 0.093 | 0.829 |
| F(000) | 1440.0 | 2808.0 |
| Crystal size/mm$^3$ | 0.21 × 0.19 × 0.16 | 0.2 × 0.19 × 0.16 |
| Radiation | MoKα (λ = 0.71073) | MoKα (λ = 0.71073) |

| | | |
|---|---|---|
| 2Θ range for data collection/° | 5.996 to 49.998 | 4.234 to 50.698 |
| Index ranges | -14 ≤ h ≤ 19, -34 ≤ k ≤ 35, -8 ≤ l ≤ 8 | -28 ≤ h ≤ 28, -15 ≤ k ≤ 15, -23 ≤ l ≤ 16 |
| Reflections collected | 10271 | 52543 |
| Independent reflections | 2837 [$R_{int}$ = 0.0935, $R_{sigma}$ = 0.1068] | 10810 [$R_{int}$ = 0.0501, $R_{sigma}$ = 0.0430] |
| Data/restraints/parameters | 2837/7/231 | 10810/0/805 |
| Goodness-of-fit on $F^2$ | 1.133 | 1.080 |
| Final R indexes [I>=2σ (I)] | $R_1$ = 0.0973, $wR_2$ = 0.1617 | $R_1$ = 0.0797, $wR_2$ = 0.1928 |
| Final R indexes [all data] | $R_1$ = 0.1336, $wR_2$ = 0.1759 | $R_1$ = 0.0990, $wR_2$ = 0.2043 |
| Largest diff. peak/hole / e $Å^{-3}$ | 0.25/-0.28 | 1.01/-1.18 |

**Table 5.2** Crystal data and structure refinement parameters for the hnmh-$PLYH_2$ ligand and complex **4** (CCDC 2304746 and 2304747).

| Identification code | hnmh-$PLYH_2$ | $[Fe^{III}_2$(hnmh-$PLY)_3]$, **4** |
|---|---|---|
| Empirical formula | $C_{96}H_{64}N_8O_8$ | $C_{72}H_{42}Fe_2N_6O_6$ |
| Formula weight | 1457.55 | 1198.82 |
| Temperature/K | 273.15 | 100 |
| Crystal system | orthorhombic | triclinic |
| Space group | $P2_12_12_1$ | P-1 |
| a/Å | 4.6410(8) | 13.2008(16) |
| b/Å | 13.252(3) | 15.706(2) |
| c/Å | 27.377(5) | 16.0595(17) |
| α/° | 90 | 81.353(4) |
| β/° | 90 | 77.826(4) |
| γ/° | 90 | 67.397(4) |
| Volume/$Å^3$ | 1683.8(5) | 2995.9(6) |
| Z | 1 | 2 |
| $\rho_{calc}g/cm^3$ | 1.437 | 1.329 |
| $\mu/mm^{-1}$ | 0.093 | 0.544 |
| F(000) | 760.0 | 1232.0 |
| Crystal size/$mm^3$ | 0.2 × 0.2 × 0.2 | 0.2 × 0.2 × 0.2 |
| Radiation | MoKα (λ = 0.71073) | MoKα (λ = 0.71073) |
| 2Θ range for data collection/° | 4.278 to 56.796 | 3.98 to 57.118 |
| Index ranges | -6 ≤ h ≤ 6, -17 ≤ k ≤ 17, -36 ≤ l ≤ 36 | -16 ≤ h ≤ 17, -21 ≤ k ≤ 21, -20 ≤ l ≤ 21 |
| Reflections collected | 23273 | 48330 |
| Independent reflections | 4229 [$R_{int}$ = 0.1155, $R_{sigma}$ = 0.0708] | 15275 [$R_{int}$ = 0.0518, $R_{sigma}$ = 0.0615] |
| Data/restraints/parameters | 4229/0/254 | 15275/0/765 |
| Goodness-of-fit on $F^2$ | 1.140 | 1.221 |
| Final R indexes [I>=2σ (I)] | $R_1$ = 0.0653, $wR_2$ = 0.1632 | $R_1$ = 0.0773, $wR_2$ = 0.1880 |
| Final R indexes [all data] | $R_1$ = 0.0966, $wR_2$ = 0.1897 | $R_1$ = 0.1027, $wR_2$ = 0.2004 |
| Largest diff. peak/hole / e $Å^{-3}$ | 0.36/-0.42 | 2.04/-0.55 |

Furthermore, the dinuclear complexes were characterized by a set of other techniques such as HRMS (High-resolution mass spectrometry), XPS (X-ray photoelectron spectroscopy), EPR (Electron paramagnetic resonance), elemental analysis, UV-vis (Ultraviolet-visible), and FT-IR (Fourier transform infrared) spectroscopy (Figures 5.2 and 5.3). X-band EPR spectrum of complexes, **3** and **4** in solid state displayed broad signal at g ≈ 2.2 and g ≈ 2.7 at room temperature. Such broad EPR resonances have been previously observed for weakly coupled diiron(III) paramagnetic complexes [Saroja et

al., 1995; Zheng et al., 2000]. XPS technique confirms the presence of the +3 oxidation state for both the Fe-centers in complexes **3** and **4**. From the Fe 2p XPS spectrum of the complex **3**, binding energies (BEs) for Fe $2p_{3/2}$ and Fe $2p_{1/2}$ spin components are obtained in the regions of 711 and 723 eV, respectively, which is a typical characteristic of Fe(III) center [İşci et al., 2009; Sun et al., 2022a]. Similarly, for complex **4**, the XPS signals for Fe $2p_{3/2}$ and Fe $2p_{1/2}$ binding energies appeared at 710, and 723 eV, respectively.

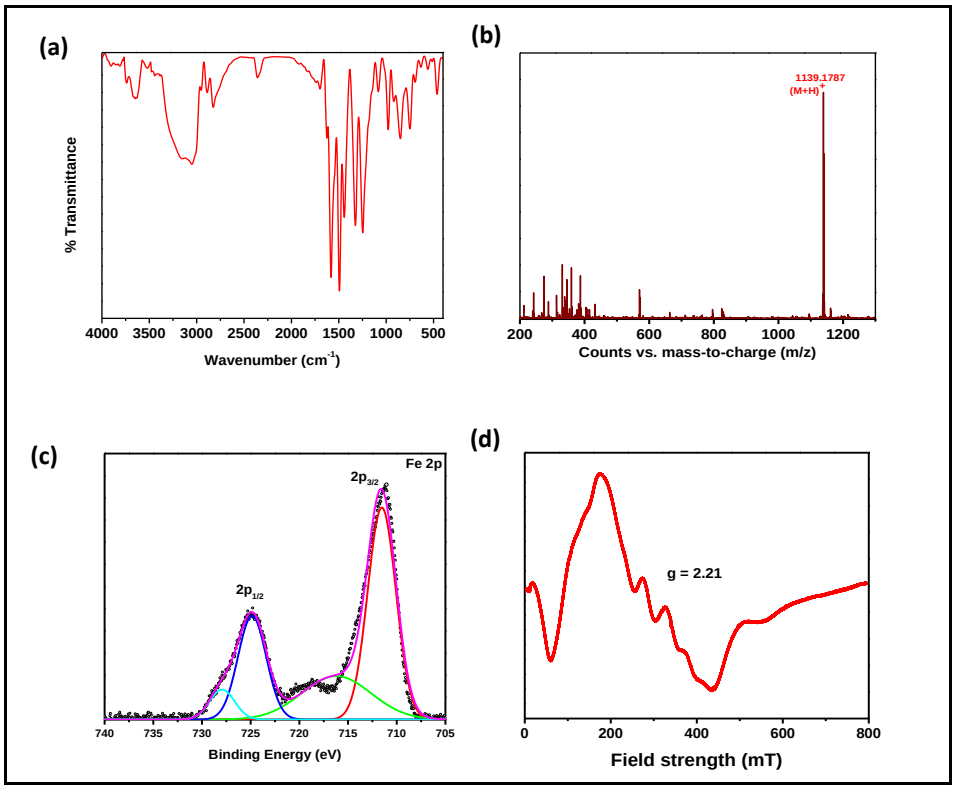



**Figure 5.2 (a)** FTIR, **(b)** HRMS, **(c)** Fe 2p XPS, **(d)** EPR spectrum of complex **3**.

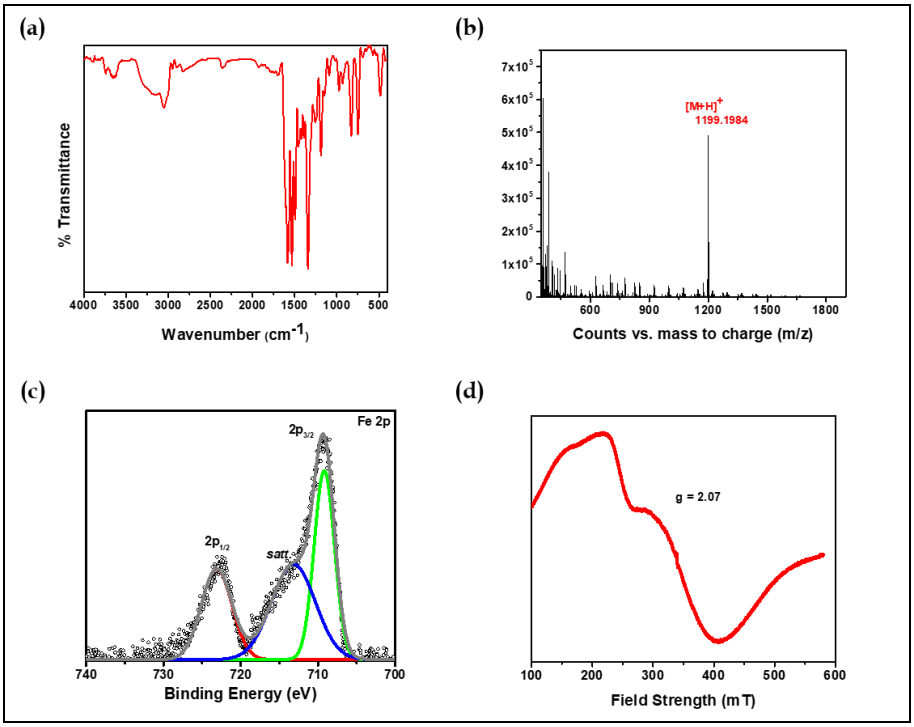



**Figure 5.3 (a)** FTIR, **(b)** HRMS, **(c)** Fe 2p XPS, **(d)** EPR spectrum of complex **4**.

### 5.3.2 Electrocatalytic Reduction of $H_2O_2$

Complexes **3** and **4** were drop cast on the surface of a glassy carbon (GC) electrode to prepare **GC-3** and **GC-4** electrodes. The electrocatalytic reduction of $H_2O_2$ was subsequently examined in a three-electrode cell; **GC-3** or **GC-4** working electrode, Pt wire counter electrode, and Ag/AgCl (3.0 M KCl) reference electrode, respectively. A detailed description of the electrode preparation is given in the experimental section. The preliminary cyclic voltammetry (CV) tests for $H_2O_2$ reduction by the **GC-3** electrode are demonstrated in Figure 5.4a. Notably, a large cathodic current with an onset potential ≈ of 0.43 V (vs. Ag/AgCl, 3.0 M KCl) was observed for **GC-3** on the addition of 0.1 M $H_2O_2$ in acetate buffer (pH 3.0) as the electrolyte.

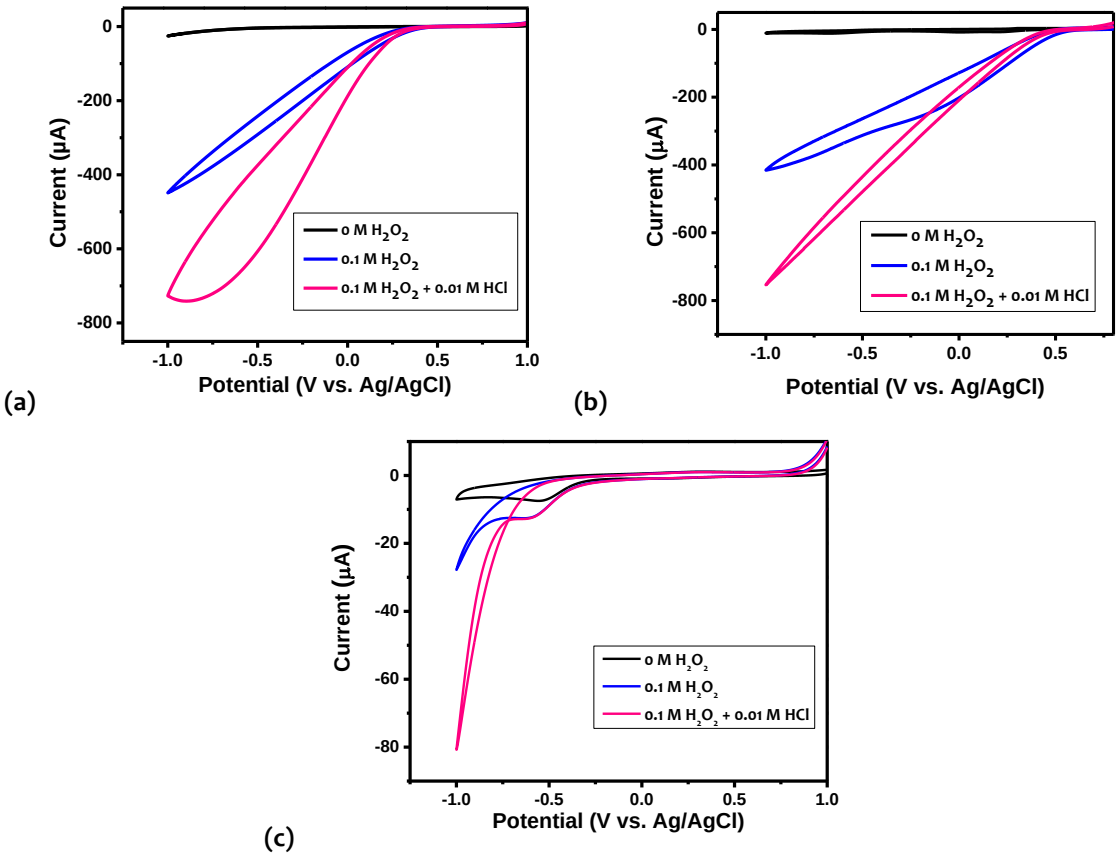


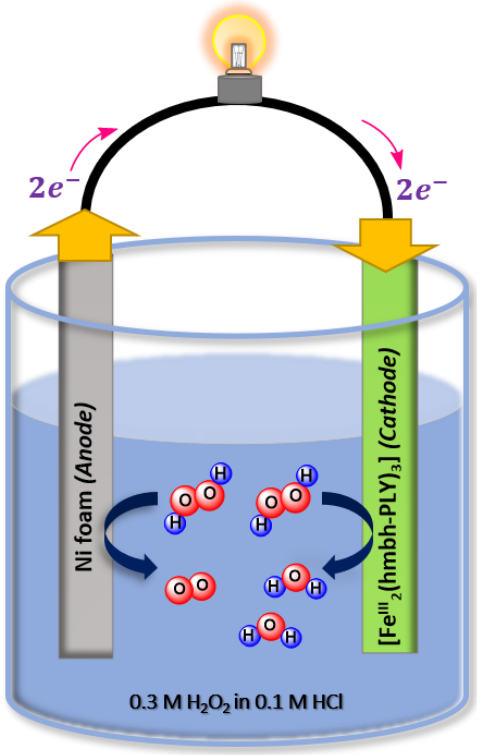

**Figure 5.4** The preliminary cyclic voltammetry (CV) tests for $H_2O_2$ reduction performed on **(a) GC-3 (b) GC-4,** and **(c)** bare glassy carbon electrode as the working electrode in acetate buffer (pH 3.0); Ag/AgCl (3.0 M KCl) as a reference, and Pt-wire as the counter electrode, at a scan rate of 100 mV $s^{-1}$.

The CV in the absence of $H_2O_2$, under identical conditions (Figure 5.4a, black curve) is provided for the comparison. To improve the current, while keeping the amount of $H_2O_2$ constant, a concurrent test with a **GC-3** working electrode in the presence of 0.01 M HCl in the acetate buffer (pH 3) was recorded. The current was gradually increased (≈ 725 µA) with a discreet change in reduction onset potential (≈ 0.40 V). Parallelly, for the **GC-4** electrode, a notable increase in cathodic current with an onset potential of 0.51 V (vs. Ag/AgCl electrode, 3.0 M KCl) was observed on the addition of 0.1 M $H_2O_2$ to the acetate buffer (pH 3.0), as shown in Figure 5.4b. The reduction onset potential for **GC-4** was 80 mV lower than that of the **GC-5** electrode, signifying the ease of $H_2O_2$ reduction on the **GC-4** electrode's surface. Further, on the addition of 0.01 M HCl to the acetate buffer (pH 3), the CV test with **GC-4** electrode also showed a noticeable increment in the cathodic current (~760 µA), whilst the reduction onset potential remained unaffected. For reference, the CV of the bare GC electrode was recorded

under identical conditions (Figure 5.4c). With these initial results, we envisioned **GC-3** and **GC-4** to be a suitable cathode for the $H_2O_2$ fuel cell.

### 5.3.3 $H_2O_2$ Fuel Cell Performance Test

The $H_2O_2$ fuel cell performance tests were conducted using the dinuclear Fe(III) complexes (**3** and **4**) modified GCE as cathode, and nickel foam as the anode at room temperature. The choice of the anode as Ni (Nickel) metal was based on the values for the onset oxidation potential of $H_2O_2$ on the electrode's surface [İşci et al., 2009; Pariyar et al., 2015; Wang et al., 2022]. The general representation of the one-compartment $H_2O_2$ fuel cell is given in Figure 5.5a. The electrolytes used for the initial performance tests were aqueous solutions of acetate buffer (pH 3.0) and 0.1 M HCl. With acetate buffer (pH 3.0) as the electrolyte, the addition of 0.3 M $H_2O_2$ resulted in a very low open circuit potential, OCP (0.11 V) for **GC-3**, and peak power density, PPD obtained was 0.70 µW $cm^{-2}$ (Figure 5.6a). Under identical conditions, with **GC-4** as the corresponding cathode, an OCP of 0.25 V, and a PPD of 2.3 µW $cm^{-2}$ were achieved (Figure 5.6b). Switching to 0.1 M HCl (a common electrolyte for one-compartment $H_2O_2$ fuel cells) [Fukuzumi et al., 2012; Sun et al., 2022b; Yamada et al., 2011, 2013, 2014], while keeping the concentration of $H_2O_2$ constant, the OCP for **GC-3** was significantly improved to 0.65 V, and the PPD of 1.15 mW $cm^{-2}$ was attained (Figure 5.5b). Parallely, under identical conditions (0.1 M HCl), the $H_2O_2$ fuel cell employing **GC-4** electrode has shown a similar OCP value of 0.65V. Whereas, for the GC-4 electrode, a higher value of PPD ≈ 1.31 mW $cm^{-2}$ was obtained (Figure 5.5c). Besides, the polarization curve obtained while running the fuel cell performance tests with **GC-3** and **GC-4** electrodes (Figures 5.6c and d) displayed resistance up to +0.40 V and +0.50 V. Therefore, improving the conductivity of these electrodes could increase the power output of the designed fuel cells.




(a)

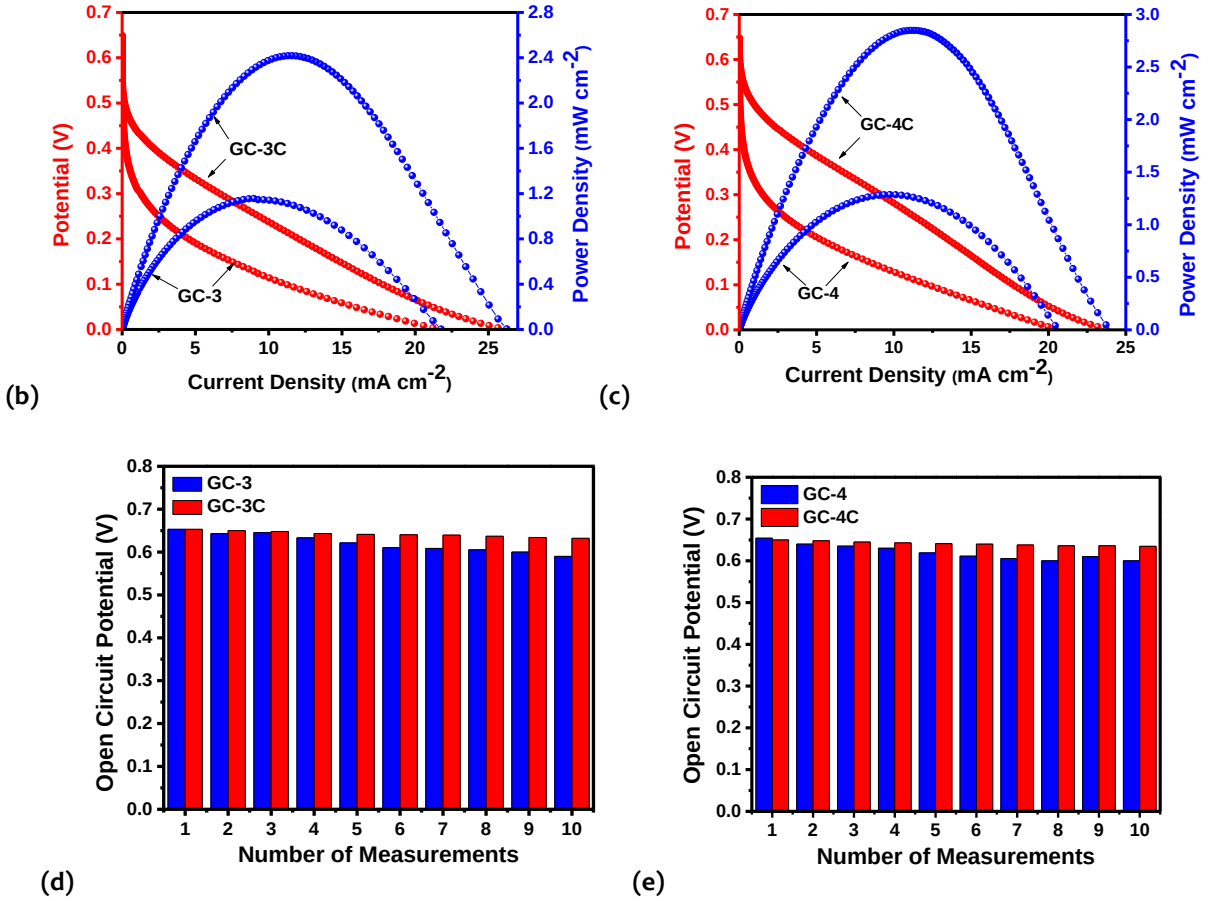



**Figure 5.5 (a)** Schematic representation of the one-compartment fuel cell with Ni foam as an anode and **GC-3** as a cathode. The *I–V* (red) and *I–P* (blue) curves obtained from the $H_2O_2$ fuel cell performance tests run in a one-compartment $H_2O_2$ fuel cell with **(b) GC-3/GC-3C** and **(c) GC-4/GC-4C** cathodes in 0.1 M HCl containing 0.3 M $H_2O_2$ and Ni foam anode, at a scan rate 10 mV $s^{-1}$. The current density is normalized to the exposed geometrical surface area of the GC electrode (0.07 $cm^{-2}$). The variation in open circuit potential (OCP) values on consecutive measurements for one-compartment $H_2O_2$ fuel cell employing **(d) GC-3/GC-3C** and **(e) GC-4/GC-4C** cathodes, and Ni foam anode in 0.1 M HCl.

Employing the cathode prepared by mixing 10% wt/wt carbon black (C) with complex **3** (**GC-3C)** in the fuel cell, under the optimized conditions (0.1 M HCl and 0.3 M $H_2O_2$), caused no change in OCP, however, a good two-fold increment in the PPD (2.41 mW $cm^{-2}$) was observed (Figure 5.5b). Adding 10% wt/wt carbon (C) to complex **4** (Figure 5.5c) for the preparation of **GC-4C** also resulted in an improvement of the conductivity of the electrode and a prominent two-fold increase in PPD (2.84 mW $cm^{-2}$) was observed. Notably, the observation from the LSV curve of **GC-3C** and **GC-4C** confirmed the improved conductance (Figures 5.6c and d). An increase in carbon percentage did not further improve the power output. The stable OCP values for 10 consecutive measurements were noticed with **GC-3C** and **GC-4C** electrodes, in comparison to that of the **GC-3** and **GC-4** electrodes (Figures 5.5d and e). The fuel cell performance of the bare GC electrode was measured under identical conditions for reference (Figure 5.6e).

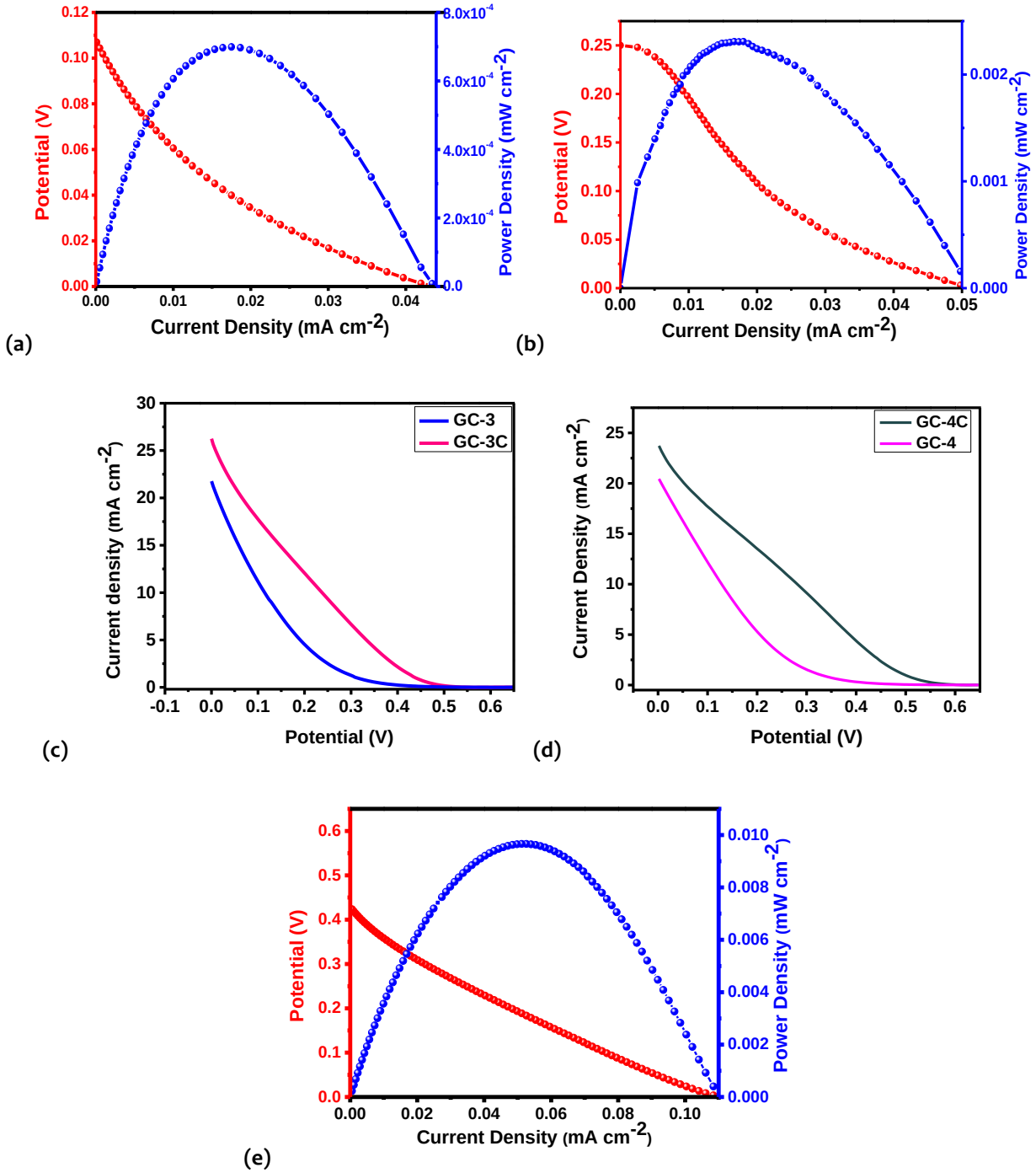



**Figure 5.6** *I-V* (red) and *I-P* (blue) curves of one-compartment $H_2O_2$ fuel cell with **(a) GC-3** and **(b) GC-4** cathode, and Ni foam anode at a scan rate 10 mV $s^{-1}$. The performance tests were conducted in an acetate buffer (pH 3) containing 0.3 M $H_2O_2$. Current density is normalized by the geometrical area of the glassy carbon electrode. Polarization curves for **(c) GC-3** (blue curve)/**GC-3C** (pink curve) and **(d) GC-4** (pink curve)/**GC-4C** (gray curve) as the cathode in 0.1 M HCl containing 0.3 M $H_2O_2$, and Ni foam as the anode in one compartment $H_2O_2$ fuel cell at a scan rate 10 mV $s^{-1}$. Current density is normalized by the geometrical area of the glassy carbon electrode. **(e)** *I-V* (red) and *I-P* (blue) curves of a one-compartment $H_2O_2$ fuel cell with bare glassy carbon (GC) cathode and Ni foam as an anode, at a scan rate of 10 mV $s^{-1}$. The performance tests were conducted in 0.1 M HCl containing 0.3 M $H_2O_2$. The current is normalized by the geometrical area of the glassy carbon electrode.

Another set of experiments in 0.05 M and 0.2 M HCl was run to check the dependence of the above-mentioned fuel cell performance on the concentration of electrolytic HCl solution. The operation of the fuel cell in lower HCl concentration, i.e., 0.05 M HCl with

**GC-3** cathode under identical conditions, decreased the OCP value to 0.57 V, thereby, decreasing the PPD to 0.27 mW $cm^{-2}$ (Figure 5.6a). Identical studies with **GC-3C** cathode displayed no change in OCP, whereas the PPD was improved to 1.09 mW $cm^{-2}$ (Figure 5.7a). Since the half-cell reaction at the cathode for $H_2O_2$ is dependent on the active $H^+$ species [An et al., 2015]; this observation can be directly related to the decrease of $H^+$ ion concentration in the solution. The fuel cell performance test in 0.2 M HCl showed OCP, 0.65 V, and PPD, 0.55 mW $cm^{-2}$ with **GC-3** cathode (Figure 5.7b). While conducting the performance tests in 0.2 M HCl, the electrolytic solution turned light green in color, which is conceivable due to the rapid electrocatalytic oxidation of the Ni foam electrode giving $Ni^{2+}$ ions into the electrolytic solution. Furthermore, the **GC-3**-modified cathode also suffered a subsequent loss of catalyst from the electrode's surface. Therefore, the power output of the fuel cell dropped in 0.2 M HCl. A similar observation was noted with the **GC-4** cathode.

Table 5.3 demonstrates the comparison of the reported Fe(III)-based molecular complexes reported in the literature for $H_2O_2$ reduction, highlighting the superior performance of the dinuclear complexes **3** and **4** towards $H_2O_2$ reduction. It can be illustrated that by increasing the electron-accepting PLY units, and Fe(III) metal centers, the electron uptake of a cathode is improved, therefore more electrons can be provided for the reduction of $H_2O_2$ at the cathode's surface. As a consequence, a significant improvement in the PPD can be noted in the designed $H_2O_2$ fuel cell. Also, when compared to the activity of Prussian blue, which is a common cathode material used in $H_2O_2$ fuel cell [Mousavi Shaegh et al., 2012], complexes **3** and **4** showed PPD of the order ≈ 1.5 and 1.7 times higher in the identically designed one-compartment $H_2O_2$ fuel cell.

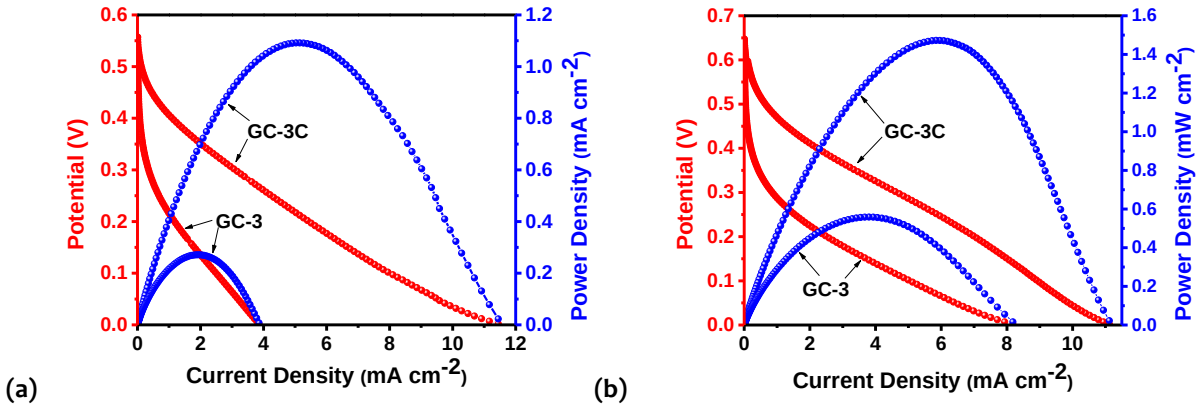



**Figure 5.7** *I-V* (red) and *I-P* (blue) curves of a one-compartment H2O2 fuel cell with **GC-3/GC-3C** cathode and Ni foam anode, at a scan rate of 10 mV $s^{-1}$. The performance tests were conducted in **(a)** 0.05 M and **(b)** 0.2 M HCl containing 0.3 M $H_2O_2$.

**Table 5.3** Comparison of the present work with the earlier reported molecular Fe(III) complexes.

| Sr. No. | Anode | Cathode | OCP (V) | PPD | References |
|---|---|---|---|---|---|
| 1 | Ni | $[Fe^{III}(Pc)Cl]$ | 0.50 | 10 μW $cm^{-2}$ | Yamada *et al.*[Yamada et al., 2011] |
| 2 | Ni | $[Fe^{III}(TPP)Cl]$ | 0.12 | > 0.03 μW $cm^{-2}$ | Yamada *et al.*[Yamada et al., 2011] |
| 4 | Ni | $[Fe^{III}(Phen)(PLY)Cl_2]$ | 0.53 | 0.61 mW $cm^{-2}$ | Pariyar *et al.*[Pariyar et al., 2015] |
| 5 | Ni | $Fe^{III}(PLY)_3$ | 0.74 | 1.43 mW $cm^{-2}$ | Pariyar *et al.*[Pariyar et al., 2015] |
| 6 | Ni | $[Fe^{III}_2(hmbh\text{-}PLY)_3]$, **3** | 0.65 | 2.41 mW $cm^{-2}$ | *This Work* |
| 7 | Ni | $[Fe^{III}_2(hnmh\text{-}PLY)_3]$, **4** | 0.65 | 2.84 mW $cm^{-2}$ | *This Work* |

### 5.3.4 Mechanistic Investigations: CV and DFT Studies

The electrochemical behavior of complexes **3** and **4** was studied by the cyclic voltammetry (CV) technique. The CV was recorded in DMF solvent, using a three-electrode cell; GC working electrode, Pt wire counter electrode, and Ag/AgCl (3.0 M KCl) reference electrode; and $Bu_4NPF_6$ (tetrabutylammonium hexafluorophosphate) as the supporting electrolyte. In complex **3,** the first two quasi-reversible reduction waves were observed at $E_1^{1/2}$ = -0.48 V ($\Delta E_1$ = 68 mV) and $E_2^{1/2}$ = -0.86 V ($\Delta E_2$ = 91 mV) (Figure 5.8), and can be assigned to the two separate reduction events at two distinct Fe-centers [Saroja et al., 1995]. On further negative potential, CV of complex **3** displayed three ligand-based quasi-reversible reductions, $E_3^{1/2}$ = -1.42 V ($\Delta E_3$ = 60 mV); $E_4^{1/2}$ = -1.97 V ($\Delta E_4$ = 96 mV); and $E_5^{1/2}$ = -2.13 V ($\Delta E_5$ = 80 mV), respectively. Complex **4** has shown a similar CV consisting of five different reduction events. The first reversible reduction event $E_1^{1/2}$ = -0.44 V ($\Delta E_1$ = 58 mV), and the second quasi-reversible reduction event at $E_2^{1/2}$ = -0.82 V ($\Delta E_2$ = 90 mV) observed in complex **4** (Figure 5.8b) corresponds to the $Fe^{III}Fe^{III}/Fe^{II}Fe^{III}$ and $Fe^{II}Fe^{III}/Fe^{II}Fe^{II}$ redox couples [Saroja et al., 1995]. The quasi-reversible reductions at further negative potentials; -1.45 V ($\Delta E_3$ = 70 mV), 1.99 V ($\Delta E_4$ = 80 mV), and -2.20 V ($\Delta E_5$ = 120 mV) can be assigned to the three PLY-based reductions.
In comparison to earlier reported $Fe(PLY)_3$ mononuclear complex [Pariyar et al., 2015], the dinuclear $Fe^{III}$-complexes reported here, in consequence of additional Fe-center, exclusively undergoes an extra reduction with an onset potential of -0.27 V to reach peak current at -0.48 V. This electrochemical behavior of complexes **3** and **4** may be directly related to the easy catalytic reduction of $H_2O_2$ and observed high power output in the $H_2O_2$ fuel cell.

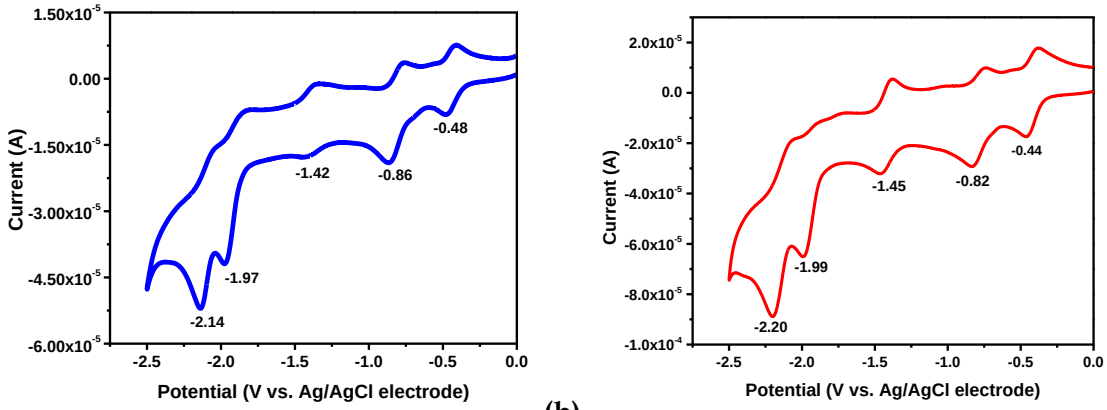



**Figure 5.8** The cyclic voltammogram of complexes, **(a) 3** and **(b) 4** obtained in DMF solvent. A scan rate of 50 mV $s^{-1}$ was maintained in a three-electrode cell; GC working electrode, Pt-wire counter electrode, and Ag/AgCl (3.0 M KCl) reference electrode [Here, L represents the coordinated (hmbh-PLY) ligand].

Further, the DFT studies were performed on complex **3** to understand the redox behavior and participation of Fe-centres in $H_2O2$ reduction. DFT computations showed that spin density calculated at the UB3LYP+D3BJ/def2-TZVP+def2-TZVPP//UB3LYP/def2-SVP+def2-TZVP level of theory for complex **3** in its high spin – high spin (HS-HS) state is primarily localized on two metal (Fe) centers; in which each metal center contributes ~42% of the total spin population. A small fraction of spin density is also observed on all six coordinated atoms (N, O), revealing good covalency in the Fe-(N/O) bonds. Note that the uncoupled triplet spin state (LS-LS) that is comprised of two low-spin ($S$ = ½) iron centers lies nearly 10 kcal/mol above the (HS-HS) spin state, and thus the HS-HS spin state is confirmed as the lowest energy spin state for complex **3** without further considering the exchange-coupling. The spin-density distribution plots

of complex **3** in its HS-HS spin state and its successive reduced species are depicted in Figure 5.9b.

By following the spin-density progression in these complexes, one can certainly conclude that the first two reductions from **3** to $\mathbf{3}^{1-}$ ($E_1^{1/2}$ = -0.48 V) and $\mathbf{3}^{1-}$ to $3^{2-}$ ($E_2^{1/2}$ = -0.86 V) are predominately Fe-centered, as where the spin population on metal centers get reduced to 38% after the two-electrons reduction. Whereas the next three reductions from $3^{2-}$ to $\mathbf{3}^{3-}$ ($E_3^{1/2}$ = -1.42 V), $\mathbf{3}^{3-}$ to $\mathbf{3}^{4-}$ ($E_4^{1/2}$ = -1.97 V), and $\mathbf{3}^{4-}$ to $\mathbf{3}^{5-}$ ($E_5^{1/2}$ = -2.13 V) are likely to be ligand-based, without making any further changes in the oxidation state of Fe centers. The emerging spin density on the ligand backbone primarily resides on the terminal C atoms of the PLY group is also observed in the previous study by Mishra *et al*. [Mishra et al., 2012]. As revealed from the MO analyses, the electron density on $\beta$-LUMO orbitals of **3** and $\mathbf{3}^{1-}$ have an appreciable metal contribution, ~ 55%, and 68%, respectively, whereas the $\beta$-LUMOs of $\mathbf{3}^{2-}$, $\mathbf{3}^{3-}$, and $\mathbf{3}^{4-}$ are predominately localized on the PLY backbones of ligand moiety. Hence, the reduction at $E_3^{1/2}$ = -1.42 V, corresponding to $\mathbf{3}^{2-}$ to $\mathbf{3}^{3-}$, generates the open-shell state of PLY, and the subsequent reductions add electrons exclusively to the other two-PLY rings. The electron reduction processes and their co-relation with DFT-generated molecular orbitals are briefed in Figure 5.9. It was also revealed from DFT calculations that the $Fe^{III}$ metal connected to two PLY backbones undergoes the first reduction at $E_1^{1/2}$ = -0.52V. It is worth mentioning that a ligand-centered reduction for the first two reductions of complex **3** cannot be completely excluded, as the $\beta$-LUMO of **3** and $\mathbf{3}^{1-}$ has nearly 45% and 33% ligand contribution, respectively. Interestingly, $\beta$-LUMO of the mixed-valent diiron complex upon spin-crossover, LS-HS ($S = 5/2$) and LS-LS ($S = 1/2$) spin states, show substantial enhancement in ligand contributions (58% - 72%) (Figure 5.9). Thus, a ligand-based chemical reactivity could be prompted by tuning the spin state of the Fe(III)-Fe(II) complex. According to our DFT computations, a very weak anti-ferromagnetic coupling, $J$ = -9.93 $cm^{-1}$, is observed in complex **3**, with the broken symmetry (BS) spin state being 0.71 kcal/mol stable than the uncoupled quintet state (S = 5). A series of diiron(III) complexes reported earlier also exhibited anti-ferromagnetic coupling between two HS iron centers [Binning Jr. et al., 2008; Guedes et al., 2013]. Analogously, the HS-Fe(II) and HS-Fe(II) ions in the two-electron reduced $\mathbf{3}^{2-}$ complex exhibit very weak anti-ferromagnetic coupling ($J$ = -12.47 $cm^{-1}$), with BS state 0.57 kcal/mol more stable than the high spin state. On the other hand, a very weak ferromagnetic coupling ($J$ = 4.13 $cm^{-1}$) is observed in $\mathbf{3}^{1-}$ (a mixed-valent $Fe^{III}Fe^{II}$ diiron complex) with the BS state lying nearly 0.24 kcal/mol above the ground electronic state ($S = 9/2$) that comprised of HS-Fe(III) and HS-Fe(II) ions. The energy difference is far below the uncertainty range of DFT computations, particularly in predicting reliable spin-state energetics of transition metal complexes [Ye et al., 2010]. The weak coupling between two iron centers may explain the agreement between the HS and BS geometries around the diiron centers. Interestingly, in reduced complex $\mathbf{3}^{3-}$, the high-spin Fe(II) ion is ferromagnetically coupled ($J$ = 39.27 $cm^{-1}$) with one ligand electron but anti-ferromagnetically coupled ($J$ = -11.22 $cm^{-1}$) with other HS-Fe(II) ion. The one-electron absolute reduction potentials are calculated for the first three successive reductions of complex **3** in an aprotic DMF solvent using the UB3LYP + D3BJ method in conjugation with def2-TZVP+def2-TZVPP basis functions. The computed absolute redox potential (ARP) values are $E^0_{1\,ARP}(abs, DMF)$ = 3.87 V, $E^0_{2\,ARP}(DMF)$ = 3.55 V and $E^0_{3\,ARP}(DMF)$ = 2.22 V for the one, two, and three-electron reductions, respectively. All participating complexes are considered in their high-spin state for redox calculations. This consideration is acceptable as the BS and HS spin states are nearly isoenergetic for these complexes. In Table 5.4, we report one-electron absolute redox-potential ($E^0_{n\,ARP}$) computed for each reduction step (n = 1, 2, 3, and 4) of four electrons reduction process of complex **3,** and the relative reduction potentials reference to $E^0_{1\,ARP}$ which then compared with the CV-acquired values of ($E_n^{1/2}$ - $E_1^{1/2}$). The second

reduction potential, which appears at -0.32 V relative to the first reduction potential (0.00 V), accords well with the CV-recorded gap between first two reduction peaks ($E_2^{1/2}$ – $E_1^{1/2}$ = -0.38 V) of complex **3**, further confirming that the first two reductions are metal-based reduction, Fe(III)/Fe(III) → Fe(III)/Fe(II) → Fe(II)/Fe(II). Surprisingly, the computed third and fourth reduction peaks appear slightly further than the experimentally recorded CV peaks. The high-spin consideration may not apply here due to significant magnetic coupling between ligand and metal electrons; thus, one must consider all possible coupling between metal-metal and metal-ligand electrons.

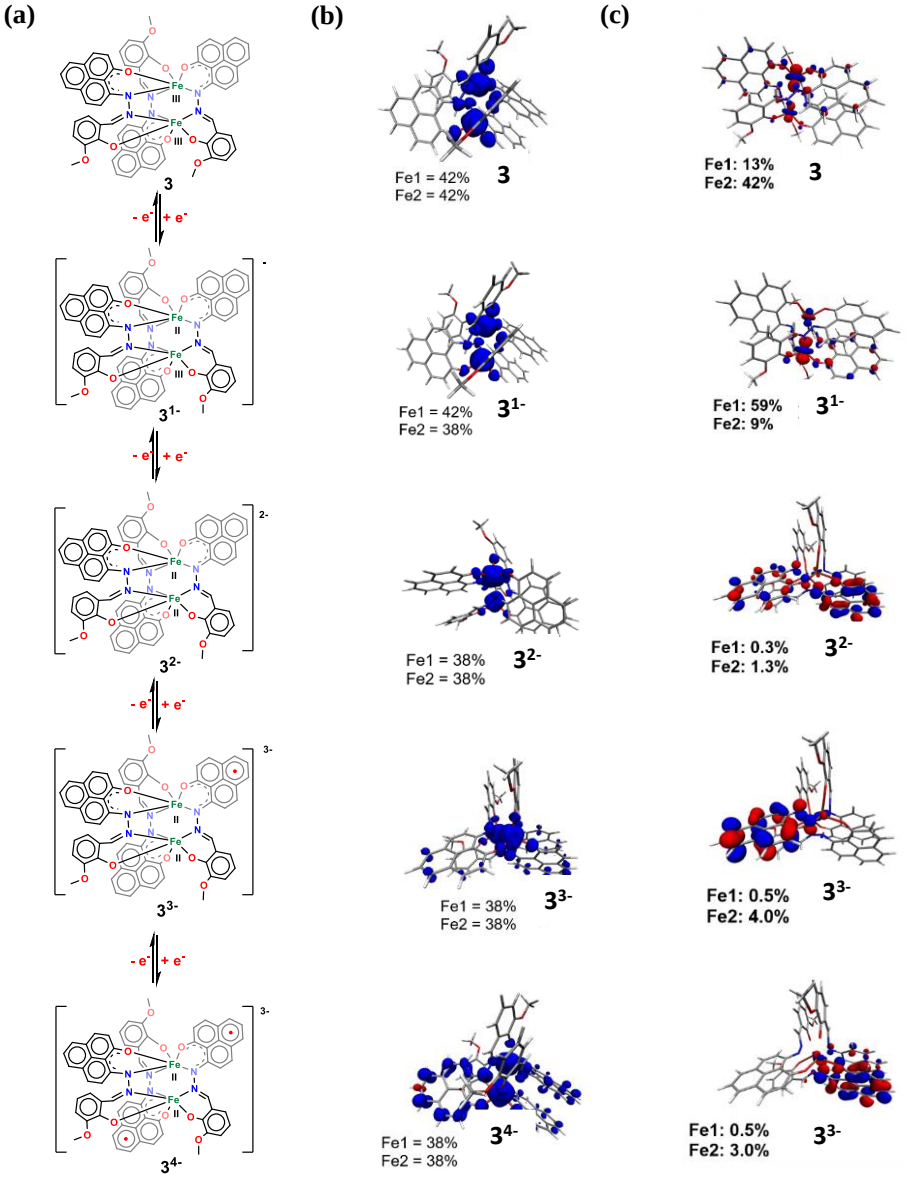



**Figure 5.9 (a)** The successive four electron reductions on complex **3**, **(b)** Spin-density and **(c)** Molecular orbital plots of β-LUMO orbitals of **3**, $3^{1-}$, $3^{2-}$, $3^{3-}$ and $3^{4-}$ complexes. Spin density plots are generated at 0.004 au ($e^2$/bohr$^4$) isosurface value (blue, α spin; red, β spin density). Molecular orbitals are generated at an isosurface value of 0.04 au. Compositions of metal ions in the β-LUMO orbital are also given for each complex.

**Table 5.4** Comparison between the theoretical and CV recorded redox peaks in DMF solvent for the successive three electron reductions of complex **3**. Calculated ARP ($E^0_{n,ARP}$) (in V) are obtained at UB3LYP + D3BJ/def2-TZVP+def2-TZVPP level of theory using a CPCM solvation model.

| Electrochemical Reductions on Complex 3 | Theoretical ARP | | Experimental RP | |
|---|---|---|---|---|
| | $E^0_{n,ARP}$ | $E^0_{n,ARP}$ - $E^0_{1,ARP}$ | $E_n^{1/2}$ | $E_n^{1/2}$ - $E_1^{1/2}$ |
| $[Fe^{III}Fe^{III}L_3]$ + $e^-$ → $[Fe^{II}Fe^{III}L_3]$ | 3.87 | 0.00 | -0.48 | 0.00 |
| $[Fe^{II}Fe^{III}L_3]$ + $e^-$ → $[Fe^{II}Fe^{II}L_3]$ | 3.55 | -0.32 | -0.86 | -0.38 |
| $[Fe^{II}Fe^{II}L_3]$ + $e^-$ → $[Fe^{II}Fe^{II}L_2L^{-\bullet}]$ | 2.22 | -1.65 | -1.42 | -0.94 |
| $[Fe^{II}Fe^{II}L_2L^{-\bullet}]$ + $e^-$ → $[Fe^{II}Fe^{II}L\,L^{-\bullet}L^{-\bullet}]$ | 1.95 | -1.92 | -1.97 | -1.49 |

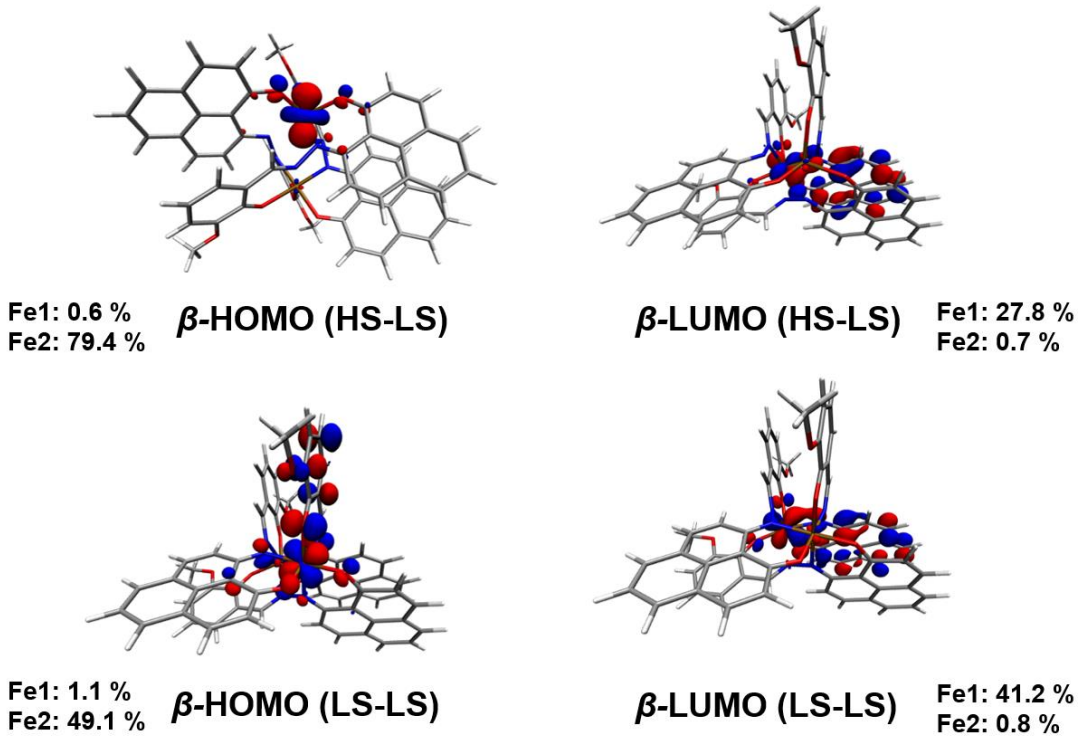



**Figure 5.10** Molecular orbital plots of *β*-HOMO and *β*-LUMO orbitals of $\mathbf{3}^{-1}$ complex in its LS-HS ($S = \frac{5}{2}$) and LS-LS ($S = \frac{1}{2}$) spin states . Molecular orbitals are generated at an isosurface value of 0.04 au. Compositions of metal ions are also given for each MO.

Based on CV measurements and DFT studies, the plausible operating mechanism for the $H_2O_2$ fuel cell reported here is proposed in Figure 5.11. It is well established that the oxidation of $H_2O_2$ at the anode can produce electrons and $H^+$ ions. The electrons, thus produced, move towards the cathode, where the catalyst, **3** gets reduced to give $\mathbf{3}^-$ species. Likewise, under the influence of high open circuit potential between the two electrodes, more electrons can reach the cathode to generate $\mathbf{3}^{2-}$ species. The two-electron reduced $\mathbf{3}^{2-}$ species can transfer two electrons to one molecule of $H_2O_2$ in the solution, which in combination with two $H^+$ ions produce two molecules of $H_2O$ (pathway I). This process is followed by the regeneration of catalyst **3**. Pariyar *et al.* reported the active participation of PLY rings in $H_2O_2$ reduction for a molecular cathode designed from a mononuclear Fe(III)-PLY complex [Pariyar et al., 2015]. They discussed the intriguing nature of cationic form of PLY ring coordinated directly to Fe-centre to accept the upcoming electrons to generate in-situ stable radical species, which can participate in

$H_2O_2$ reduction. Therefore, for the identically designed cathode with the dinuclear Fe(III) complex reported herein, there is a possibility for the active $\mathbf{3}^{2-}$ species (with cationic closed-shell PLY backbone) to accept at least two more electrons, giving $\mathbf{3}^{4-}$ species (with open-shell di-radical PLY backbone). The active $\mathbf{3}^{4-}$ species can donate four electrons in a single step. As a consequence, two molecules of $H_2O_2$ can be simultaneously reduced; giving four molecules of $H_2O$ and the catalyst **3** is regenerated (pathway II). The regeneration of the catalyst is confirmed by recording the UV-vis spectra of the recovered catalyst post three cycles of repetitive measurements (Figure 5.12).

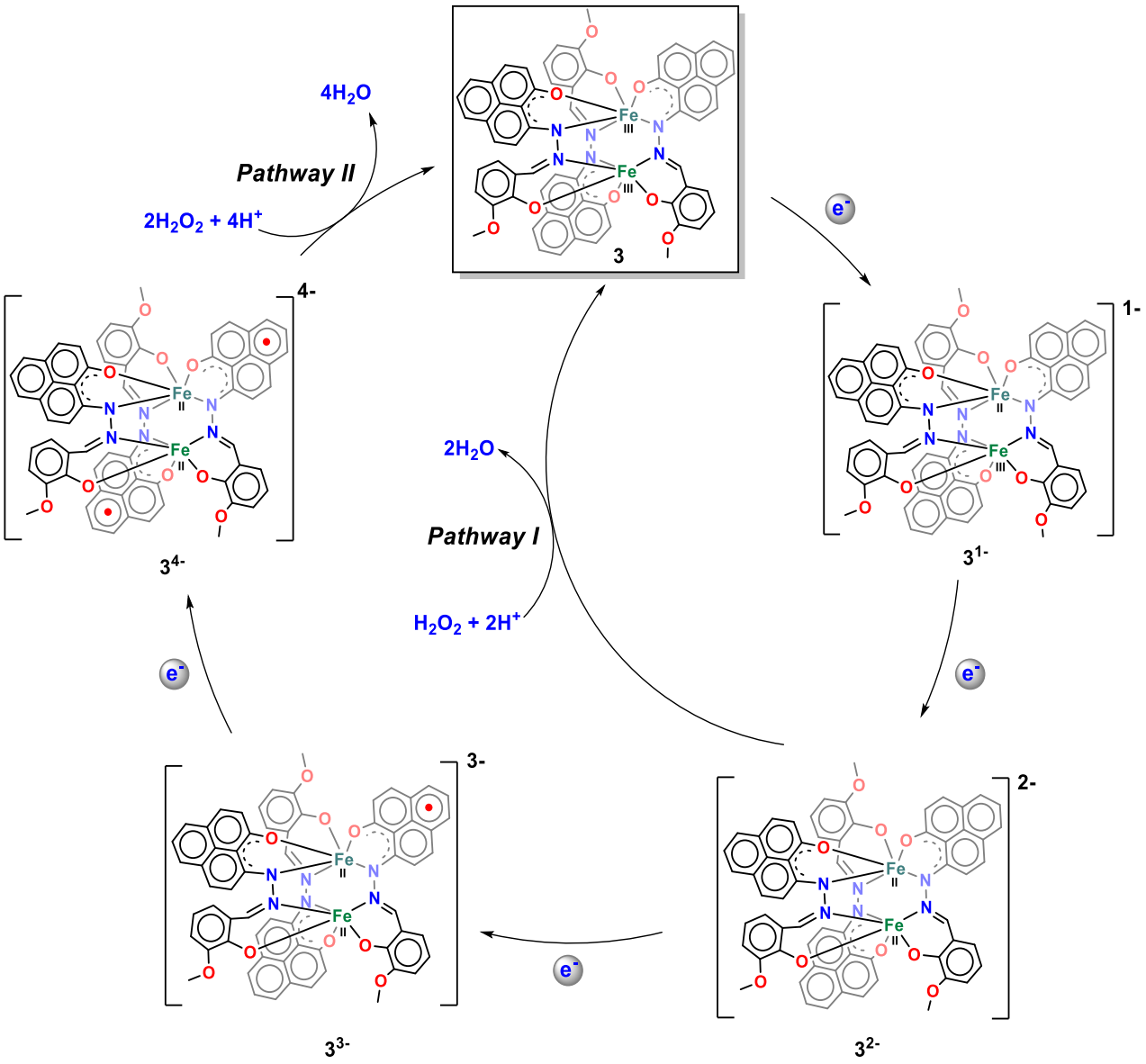



**Figure 5.11** Plausible operating pathways for the electrocatalytic reduction of $H_2O_2$ with complex **3** employed as the cathode.

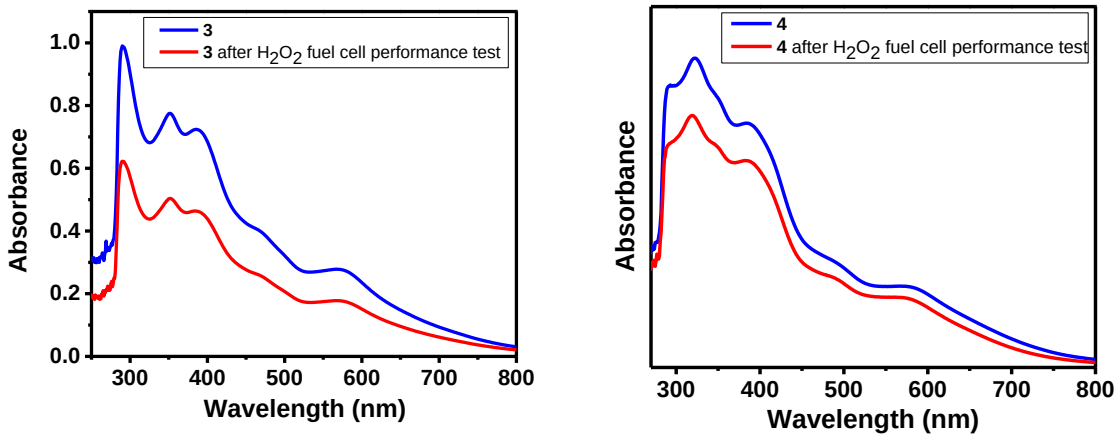
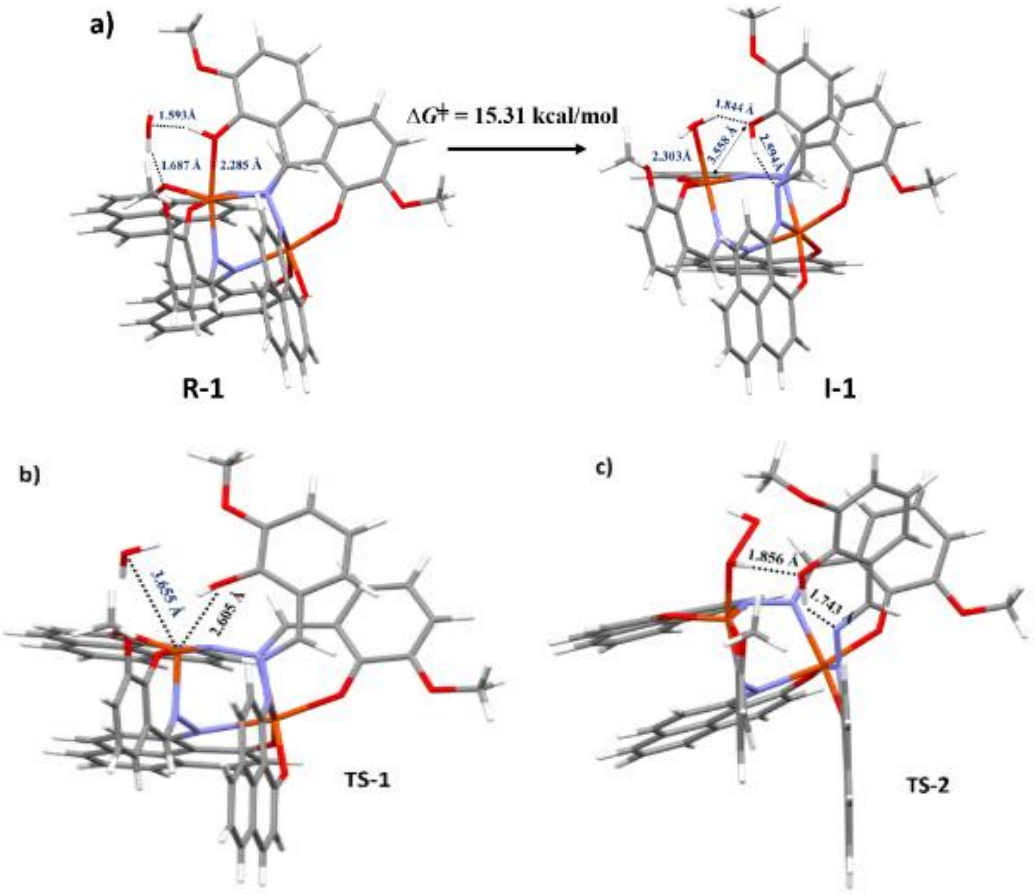



**Figure 5.12** UV-vis spectra of **(a)** complex **3** and the recovered complex from **GC-3** electrode **(b)** complex **4** and the recovered complex from the **GC-4** electrode after running the $H_2O_2$ fuel cell test.

The CV studies suggest that the two-electron reduction of $H_2O_2$ by complex **3** can proceed via ECEC and EECC (E = electron transfer, and C = chemical reaction) pathways. However, in the present study, we have investigated the mechanistic aspects of EECC pathway (pathway I) for electrochemical reduction of $H_2O_2$ in the presence of $\mathbf{3}^{2-}$ using the DFT computations. Understandably, the catalytic reduction of the $H_2O_2$ molecule requires it to be coordinated with the Fe(II) ion by replacing the solvent (water) molecule that is already non-covalent bonded with the Fe(II) ions of the $\mathbf{3}^{2-}$ complex. As reported by Yamada *et al.*, the higher average number of coordinating water molecules to the Fe ions resulted in the higher performance of an $H_2O_2$ fuel cell [Yamada et al., 2013]. Therefore, the interaction between water and Fe(II) ions plays a crucial role in $H_2O_2$ activation and, subsequently, its reduction to produce two water molecu les in an acidic medium. According to DFT calculations, the complete substitution of tetra-dentate ligand (L) by four water molecules, $[Fe^{II}Fe^{II}L_3] + 4\ H_2O \rightarrow [Fe^{II}Fe^{II}L_2 \ldots 4H_2O] + L^-$ is a highly endothermic process, $\Delta G$ = 50.97 kcal/mol. Whereas the partial substitution of ligand by water has appeared to be thermodynamically feasible, the respective pathway is studied here. It is observed that to accommodate the reactant molecule ($H_2O_2$), the two-electron reduced $\mathbf{3}^{2-}$ undergoes a structural reorganization in an acidic medium and creates a vacant coordination site on Fe(II) center. The process is first initiated by the protonation at the Fe(II)–bound oxygen site of $\mathbf{3}^{2-}$ and then forms a stable intermolecular H-bonded complex with water (solvent) molecule **(R – 1)**. This step is exothermic with $\Delta G$ = -21.28 kcal/mol. Preliminary calculations carried out using the semiempirical tight-binding method GFN2-xTB reveal that the protonation at the O(VAL), (O-atom of the o-vanillin) site of the ligand backbone is nearly 2.03 kcal/mol stable than that of the O(PLY) site and the bond dissociation of the Fe(II) – O bond occurs at lower energy than that of the Fe(II) – N bond. Additionally, DFT-optimized Fe – O/Fe – N bond distance values of **3**, $\mathbf{3}^{1-}$, and $\mathbf{3}^{2-}$ complexes unveil that the Fe – O bonds ($<R_{Fe-O}>$: 1.945 → 2.06 Å) weaken upon successive reductions of complex **3**, whereas the Fe – N bonds remain nearly unchanged ($<R_{Fe-N}>$: 2.20 Å) in the process, implies that the vacant coordination site on Fe(II) is created preferably by the Fe – O(VAL) bond dissociation. The stable intermolecular hydrogen-bonded **(R – 1)** complex then undergoes a structural reorganization to form a distorted TBP geometry Fe(II) – bound solvent (water) adduct **(I – 1)**, in which two hydrogen bonding, as shown in Figure 5.13a, provides extra stability to the solvent adduct. A dynamic equilibrium ($\Delta G^0$ = 0.1 kcal/mol) is established between the end geometries of the structural reorganization process, wherein the latter is only 0.7 kcal/mol more stable than the former. In agreement with the existence of

dynamic equilibrium, the transition state **(TS – 1)** for the reorganization of complex **(R – 1)** presents a barrier of +16.20 kcal/mol ($\Delta G^{\ddagger}$ = 15.31 kcal/mol), further supporting the existence of the room-temperature equilibrium. The optimized geometry of the transition state is depicted in Figure 5.13b. Once the solvent-bound complex is formed, $H_2O_2$ replaces the solvent molecule and bounds to the Fe(II) center. $\Delta G$ for the above solvent exchange reaction is calculated as -0.29 kcal/mol. The activated $H_2O_2$ **(R – 2)** then dissociates to produce Fe(II) – OH **(P)** and OH•. The barrier energy for the corresponding dissociation process is calculated as +14.82 kcal/mol ($\Delta G^{\ddagger}$ = +12.39 kcal/mol), and the related transition state structure (**TS – 2**) is shown in Figure 5.13c. The distal OH• migrates to the other Fe(II) center and undergoes one-electron reduction and protonation, leading to the release of a water molecule and the formation of a Fe(III) center in the complex **(Q)**. The complex **(Q)** then undergoes further one-electron reduction and protonation to produce a water molecule and diiron(III) complex. Interestingly, the H-O(VAL) site of ligand moiety or acidic electrolyte (HA) can act as a proton donor to the HO-Fe(II) site. However, the reduction and protonation step involving HA is highly endergonic ($\Delta G$ = + 88.83 kcal/mol, $S$ = 5), thus confirming an intra-proton transfer mechanism wherein the proton transfer from the H-O(VAL) site to OH-Fe(II) site of the metal complex. The O(VAL) rebounds instantly after releasing $H_2O$ to stabilize the Fe – complex and regenerate the electrocatalyst complex **3**. This step is energetically favored by $\Delta G$ = -16.40 kcal/mol. Based on the above discussion, a plausible mechanism supporting pathway I is derived for $H_2O_2$ reduction by $\mathbf{3}^{2-}$ in an acidic medium and shown in Figure 5.13d.



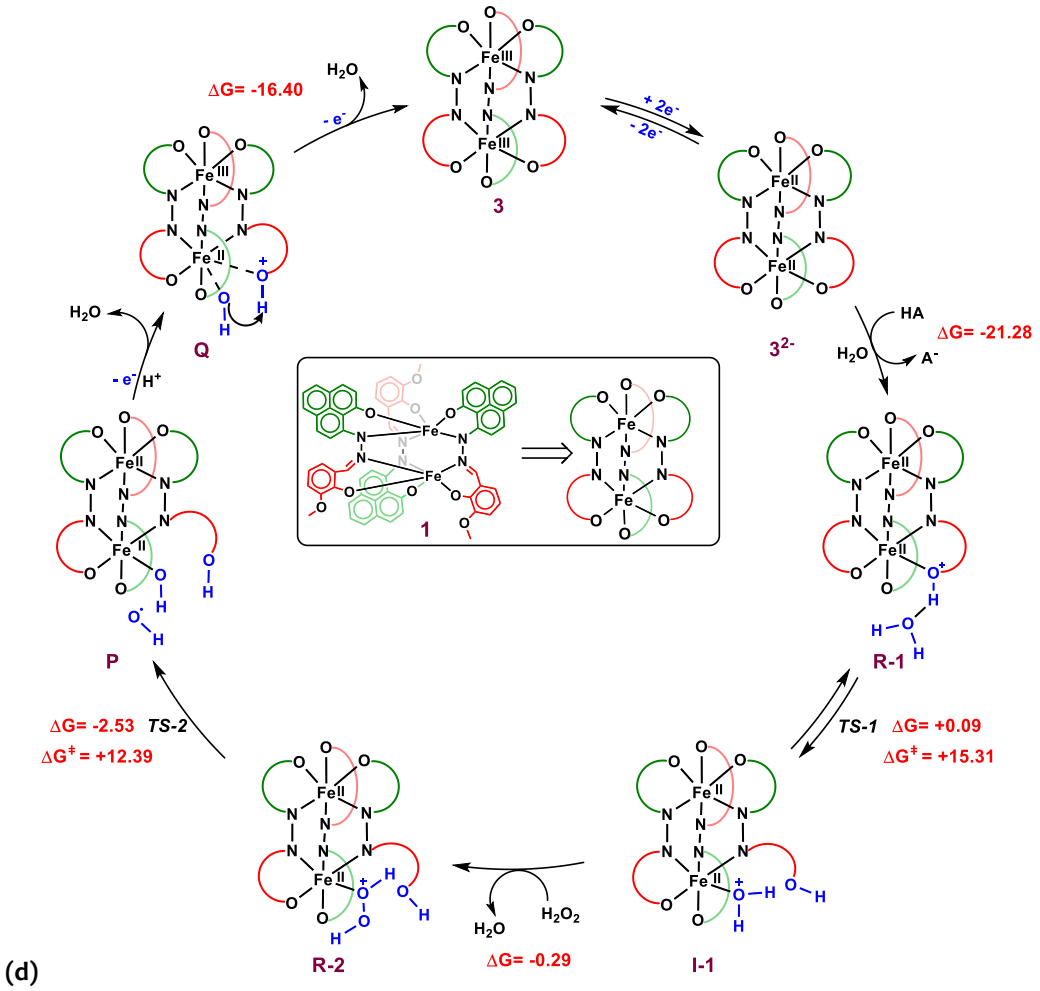



**Figure 5.13** **(a)** Structural reorganization of the intermolecular H-bonded complex **[$3^{2-}H^{+}$... $H_2O$] (R – 1)** to water-bounded Fe(II) complex **(I – 1). (b)** Molecular geometry of transition state **(TS – 1),** and **(c) (TS – 2). (d)** DFT computed mechanistic investigations for pathway I for $H_2O_2$ reduction over the Fe-centers. The energy values are given in kcal/mol.

### 5.3.5 Effect of Ligand Design on the $H_2O_2$ Fuel Cell Performance

The power output (PPD) obtained in one compartment $H_2O_2$ fuel cell with complex **3** (without C) as cathode, and Ni foam as an anode was 1.15 mW $cm^{-2}$ in 0.1 M HCl and 0.3 M $H_2O_2$. While, under identical conditions, the GC electrode modified with $[Fe^{III}_2(hnmh\text{-}PLY)_3]$ complex, **4** afforded a power output of 1.31 mW $cm^{-2}$. For both the complexes, the obtained PPD displayed a two-fold (≈ 2.2 times) increment on the addition of 10% wt/wt C, because of the improved conductivity. In this regard, we intend to highlight that the choice of aldehyde to functionalize the Hz-PLY reactant plays a vital role in improving the activity of similarly designed dinuclear iron(III) complexes towards $H_2O_2$. From the comparison of preliminary tests to check the catalytic activity of complex **3** and **4**, the onset potential for the reduction of $H_2O_2$ in acetate buffer in a three-electrode cell was recorded at 0.43 V, and 0.51 V, respectively. The ease of $H_2O_2$ reduction by complex **4** (by a factor of 80 mV) can be the contributing factor for improving the power output in the fuel cell presented here, in comparison to the fuel cell reported earlier with complex **3** as a cathode [Yamada et al., 2011, 2013].

On the other hand, the solid-state packing of PLY-derived molecules has been widely explored to understand the electron transfer mechanisms in conductors as well as electronic devices [Chi et al., 2002; Pal et al., 2004; Raman et al., 2013]. The planar PLY systems behave as a nano-graphene fragment and are well-known to show intriguing supramolecular π-π stacking in the solid state, which can facilitate the charge transfer process on a molecular level [Ahmed et al.,

2022]. In our recent report, we discussed the role of intermolecular π-π interactions between the PLY rings in a [$Co^{II}L$] ($LH_2$ = *9,9'-(Ethane-1,2-diylbis(azanediyl))bis(1H-phenalen-1-one),* complex **1** for contributing towards the low-voltage switching potential in a solid-state resistive memory device [Kamboj et al., 2023a]. The molecular structure of complex **4** in the solid state also showed very intriguing intramolecular π-π stacking interactions between the conjugated aromatic rings of the PLY-derived ligand. Three different π-π interactions were observed: a face-to-face π-π overlap of three aromatic rings of the PLY units [3.605(4) Å, 3.639(4) Å, 3.748(4) Å]; b, face to face overlap of both the aromatic rings of naphthyl units [3.873(4) Å, 3.777(4) Å]; and c, face to face overlap of one aromatic ring of the naphthyl unit [3.655(3) Å], between the (hnmh-PLY) ligands attached to the two different Fe(III) centers (Figure 5.20a). Constable *et al.* discussed the role of similar intramolecular π-π stacking interactions (face-to-face overlap) in Ir-coordinated phenyl rings for improving the performance of light-emitting electrochemical cells [Costa et al., 2010]. Very recently, Yang *et al.* reviewed that the presence of such intramolecular interactions can enhance the electron-accepting tendency of molecules, and also stabilize the excessive electronic charge via extensive delocalization [Huang et al., 2021a]. In the present instance, the supramolecular assembly in complex **4** generated by strong intramolecular π-π stacking can be advantageous in stabilizing the upcoming electrons from the Ni foam anode in an $H_2O_2$ fuel cell, through the enhanced delocalization. The solid-state molecular structure of complex **3,** in Figure 5.14, lacks the presence of such extended intramolecular π-π stacking interactions.

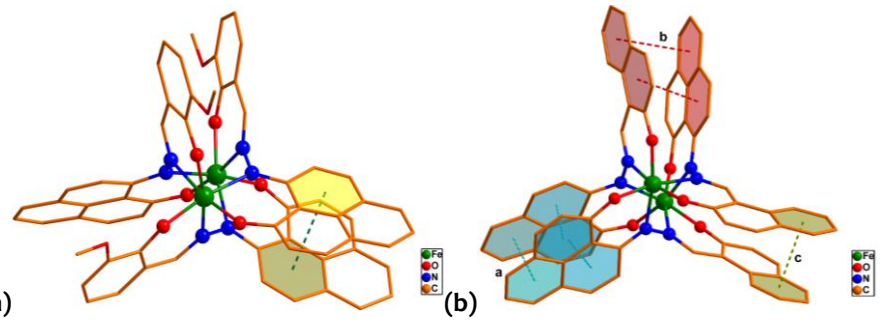



**Figure 5.14** Intramolecular π-π stacking interactions present in complexes, **(a) 3** and **(b) 4**.

Further, the solution-state CV of complex **3** displayed the first two Fe-centered reduction events $Fe^{III}Fe^{III}/Fe^{II}Fe^{III}$ and $Fe^{II}Fe^{III}/Fe^{II}Fe^{II}$ at $E_1^{1/2}$ = −0.48 V ($\Delta E_1$ = 68 mV, quasireversible) and $E_2^{1/2}$ = −0.86 V ($\Delta E_2$= 91 mV, quasireversible), respectively. Whereas for complex **3**, under identical conditions, the respective reduction events are observed at $E_1^{1/2}$ = -0.44 V ($\Delta E_1$= 58 mV, reversible), and the $E_2^{1/2}$ = -0.82 V ($\Delta E_1$= 90 mV, quasireversible). Further, we compared the obtained solid-state CV of both complexes in 0.1 M HCl electrolyte (Figure 5.15). The CV test was run in the potential widow (0.65 to 0 V) employing the one-compartment $H_2O_2$ fuel cell test experiments. **GC-3** showed a broad reduction event at a peak potential of 0.15 V vs. Ag/AgCl electrode. Whereas the CV recorded for the **GC-4** electrode has shown an early electrochemical reduction event, with a peak potential of 0.37 V vs. Ag/AgCl. The CV data (in solution as well in solid state) signifies a decrease in reduction potentials for complex **4** in comparison to complex **3**, because of the presence of intramolecular aromatic π – π stacking interactions.

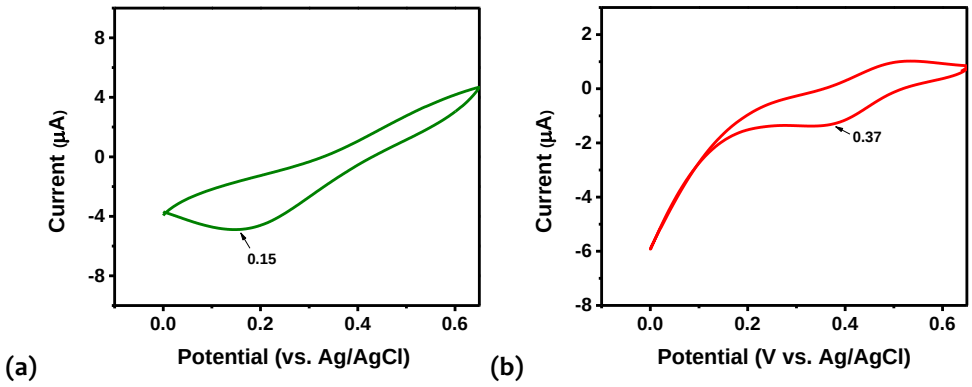



**Figure 5.15** Solid-state CV of the complexes, **(a) 3** and **(b) 4** immobilized over GCE in 0.1 M HCl electrolyte.

### 5.4 $H_2O_2$ Fuel Cell Demonstration Test

For testing the application of complex **4** modified cathode in the one-compartment $H_2O_2$ fuel cell, a demonstration setup is designed. Four beakers containing 0.3 M $H_2O_2$ in 0.1 M HCl electrolyte are connected in a series setup using the conducting copper wire through the Ni foam as anode and **GC-4C** as the cathode. The OCP for the three setups in series is measured as ~2.5 V with a multimeter. As shown in Figure 5.21, the current flow in the designed $H_2O_2$ fuel cell setup has successfully glowed a red LED (light emitting diode, 2 V) bulb, as a consequence of the reactions at the cathode and anode's surface.

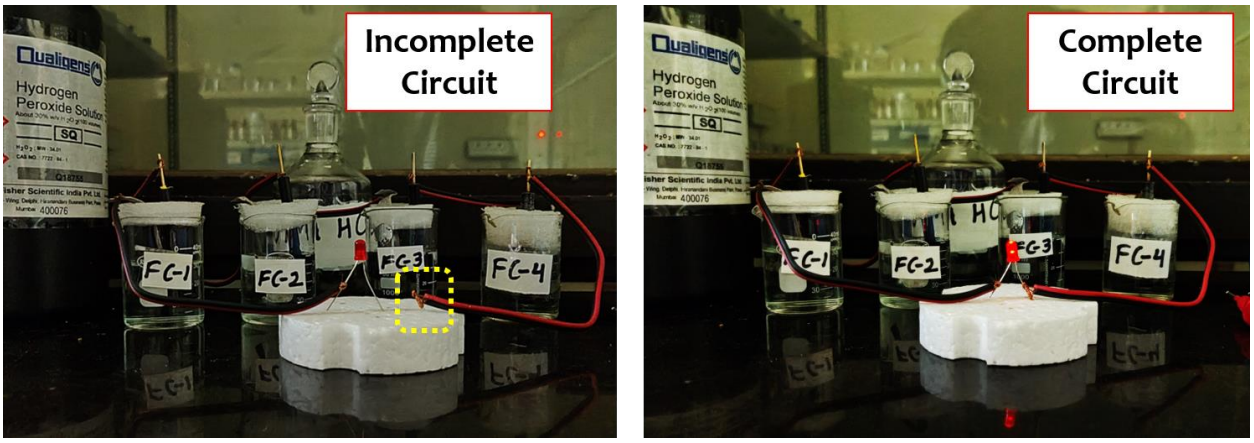



**Figure 5.16** Demonstration setup of the $H_2O_2$ fuel cell employing complex **4** as cathode and Ni foam as an anode.

### 5.5 Summary

The research findings described herein highlight a novel synthetic pathway for the rational derivatization of PLY synthon, *9-hydroxy-1H-phenalen-1-one* to a more reactive *9-hydrazineyl-1H-phenalen-1-one* (Hz-PLY) derivative. Functionalization of Hz-PLY with *2-hydroxy-3-methoxybenzaldehyde* and *2-hydroxy-1-naphthaldehyde* generated the first series of Schiff base types of ligand reported on the PLY architecture. Judicious ligand design reported herein ensured the formation of dinuclear iron(III) complexes, **3** and **4**. One compartment $H_2O_2$ fuel cell constructed with Ni-foam as anode and complex **4** as a cathode in 0.1 M HCl resulted in PPD of 2.84 mW $cm^{-2}$, which is highest in comparison to all the previously reported Fe(III)-based molecular complexes. The synergic cooperation between the PLY rings of the ligand, and the Fe(III) ions resulted in efficient $H_2O_2$ reduction in the fuel cell. Furthermore, the role of ligand substitution in enhancing $H_2O_2$ reduction is discussed.

## 5.6 Appendices

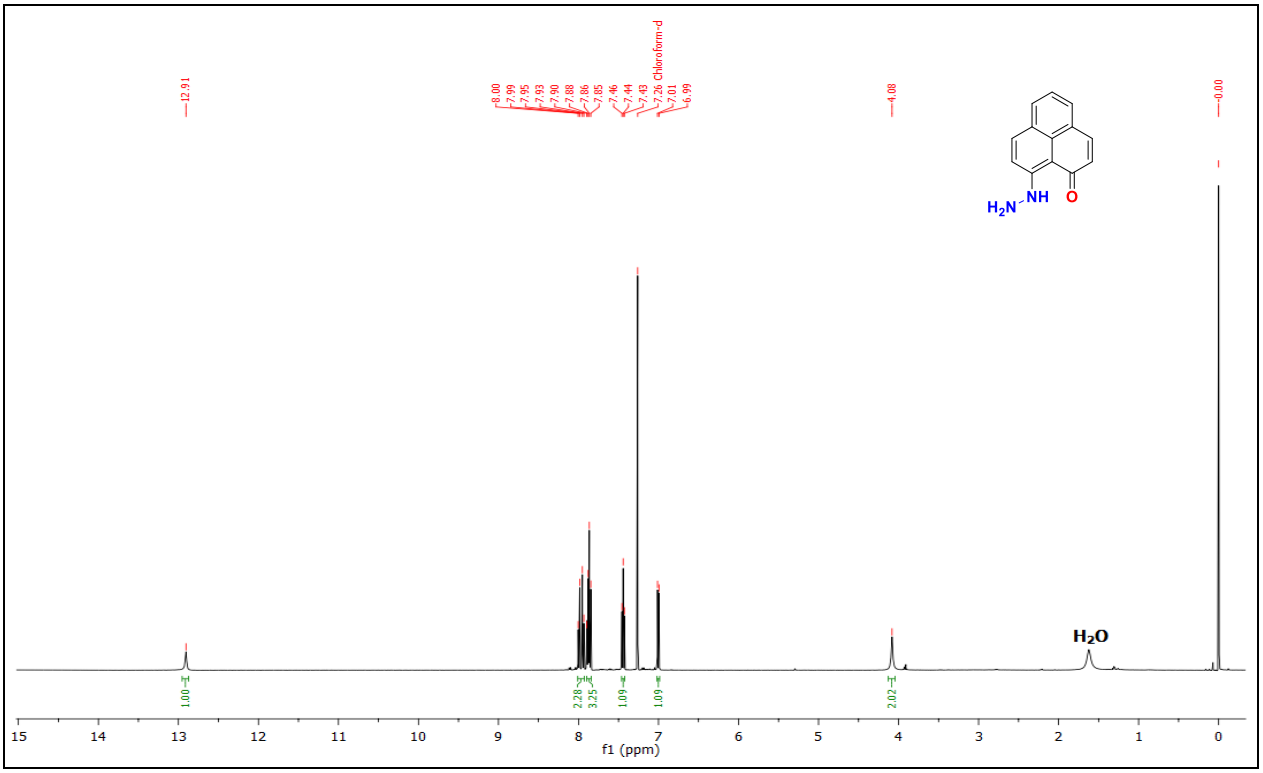



**Figure 5.17** $^{1}$H NMR of Hz-PLY recorded in $CDCl_3$ solvent.

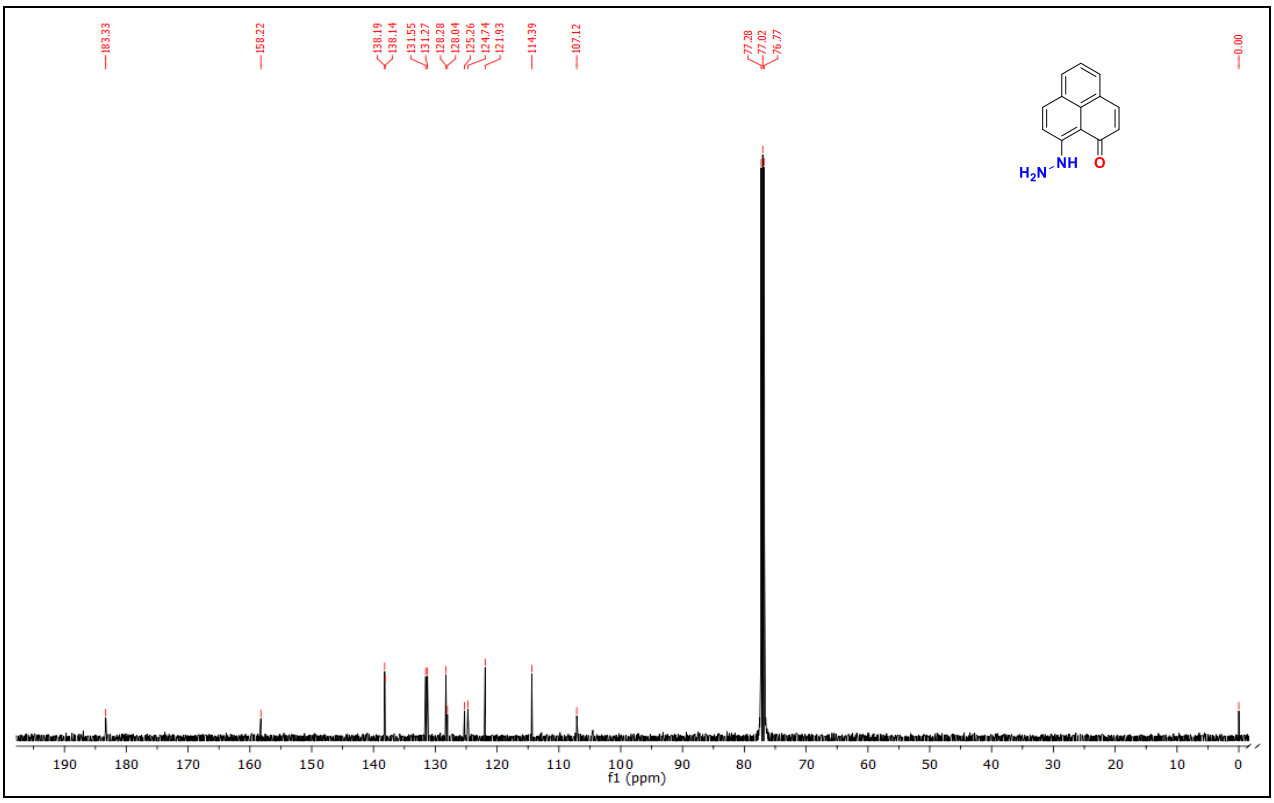



**Figure 5.18** $^{13}$C NMR of Hz-PLY recorded in $CDCl_3$ solvent.

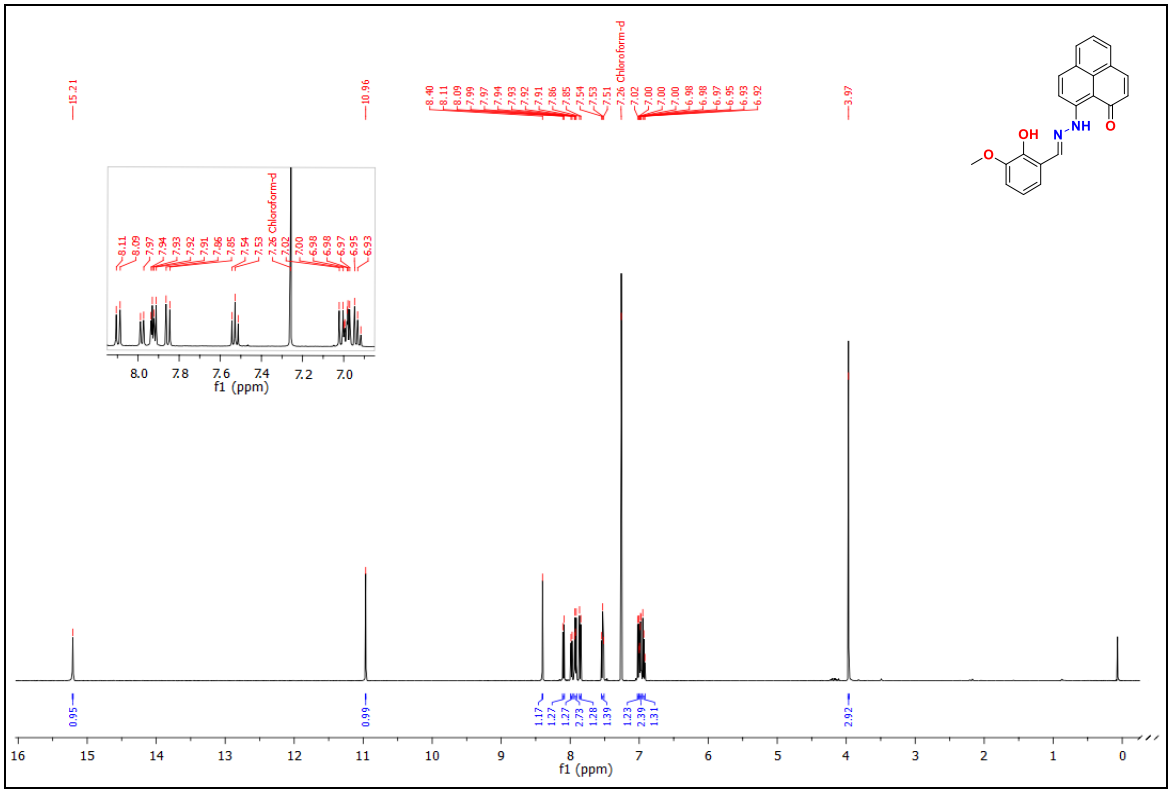



**Figure 5.19** $^{1}H$ NMR of hmbh-PLYH$_2$ recorded in $CDCl_3$ solvent.

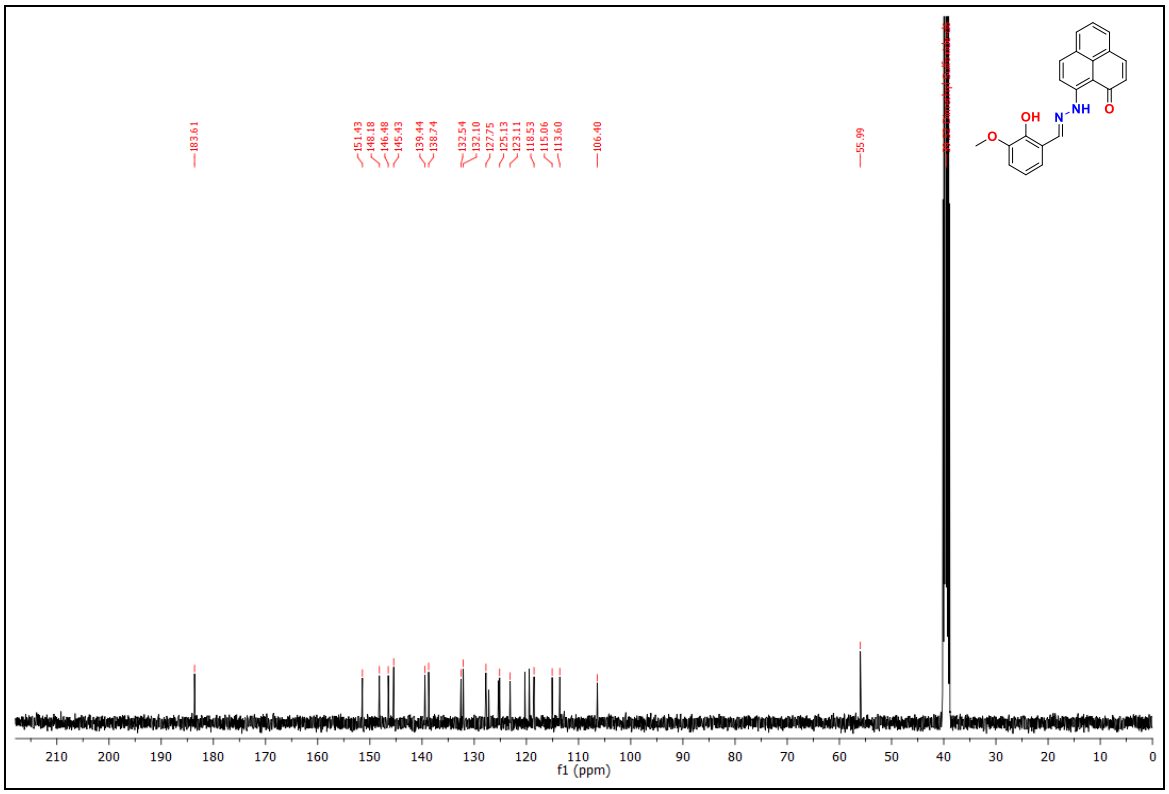



**Figure 5.20** $^{13}C$ NMR of hmbh-PLYH$_2$ recorded in $CDCl_3$ solvent.

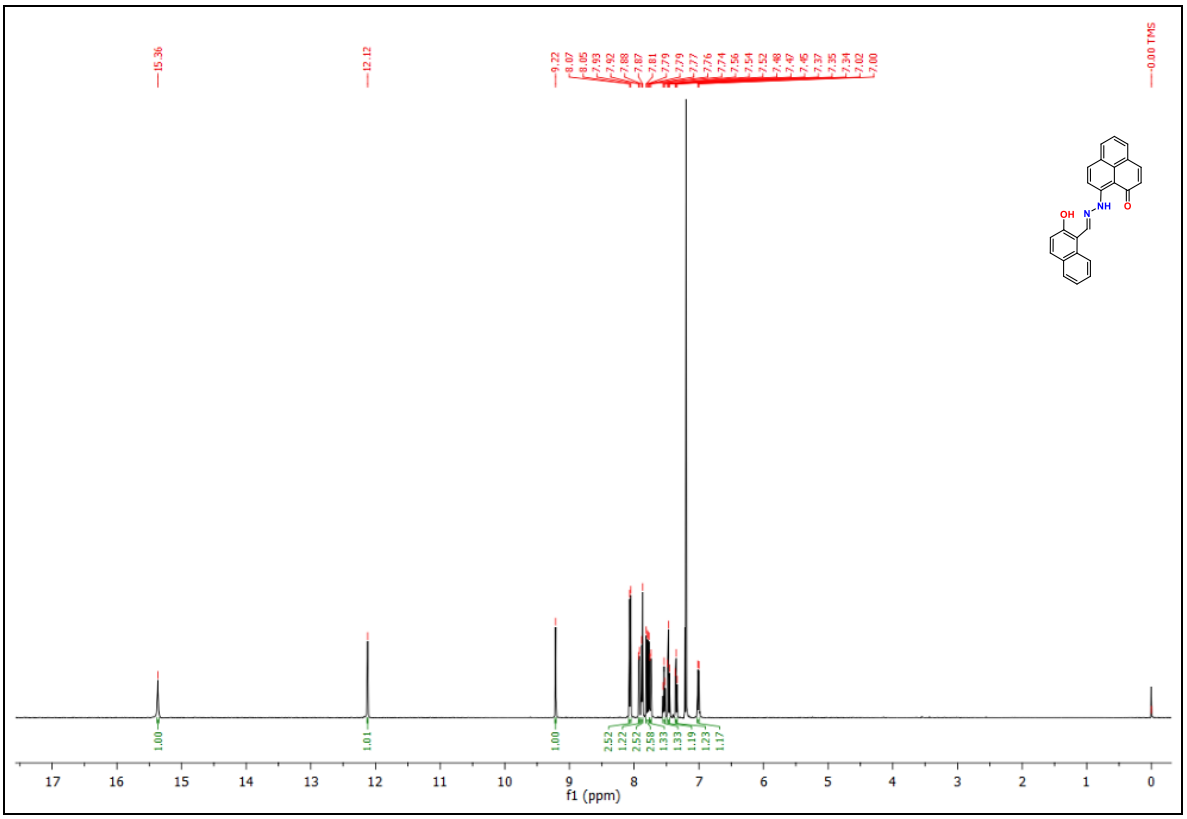



**Figure 5.21** $^{1}H$ NMR of hnmh-PLY$H_2$ recorded in $CDCl_3$ solvent.

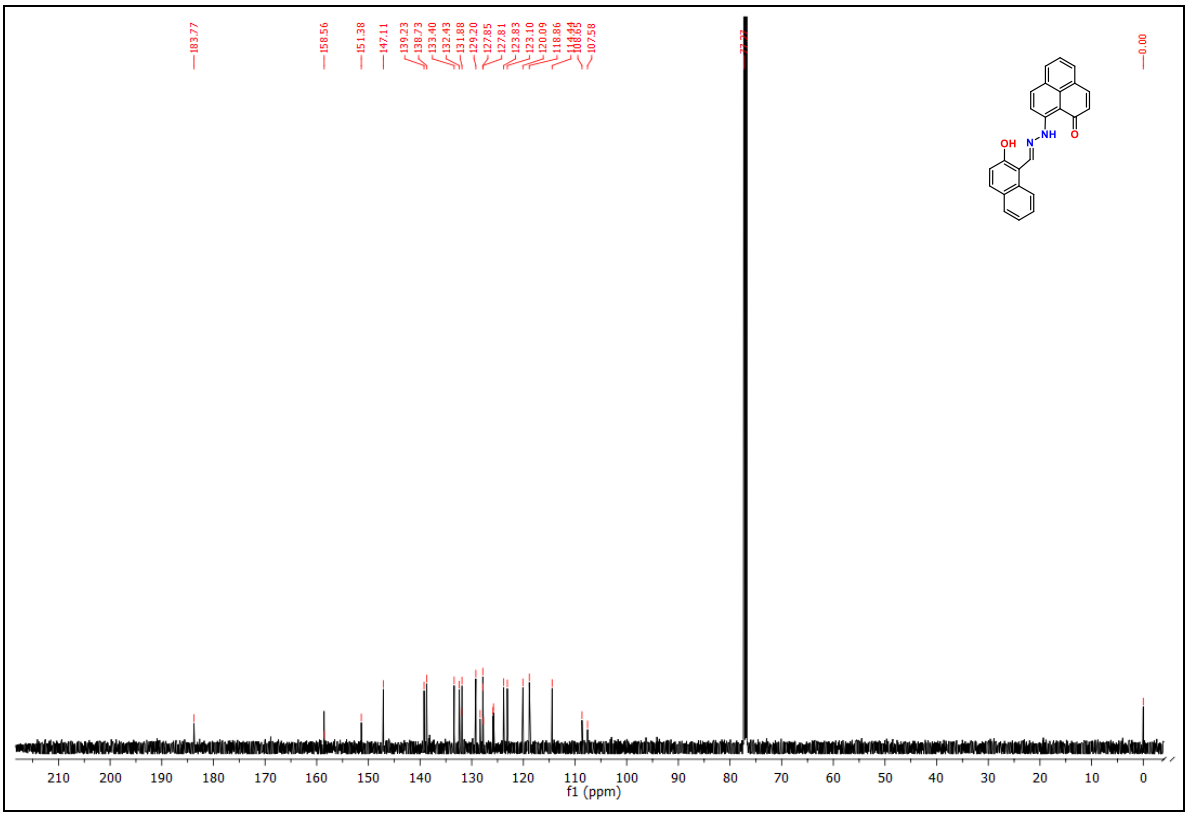



**Figure 5.22** $^{13}C$ NMR of hnmh-PLY$H_2$ recorded in $CDCl_3$ solvent.

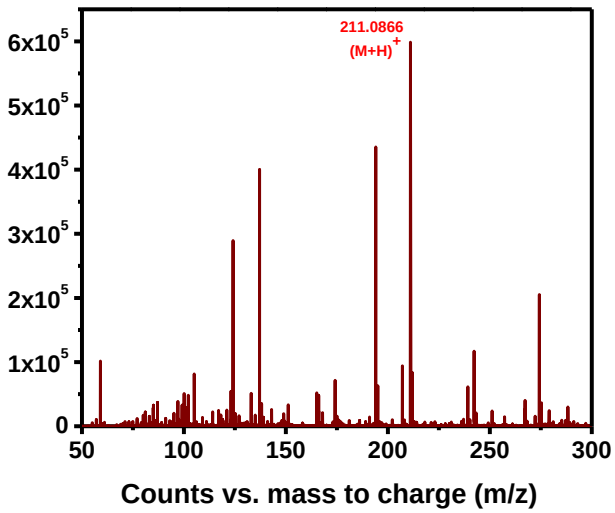



**Figure 5.23** HRMS spectrum of Hz-PLY. HRMS ($CH_3CN$, positive ionization): calcd. for $C_{13}H_{10}N_2O$ m/z = 211.0866 $[M + H]^+$, found 211.0867 $[M + H]^+$.

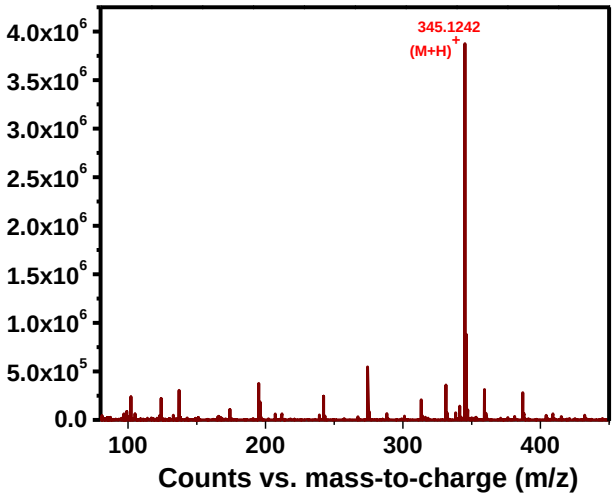



**Figure 5.24** HRMS spectrum of hmbh-$PLYH_2$. HRMS ($CH_3CN$, positive ionization): calcd. for $C_{21}H_{16}N_2O_3$ m/z = 345.1234 $[M + H]^+$, found 345.1242 $[M + H]^+$.

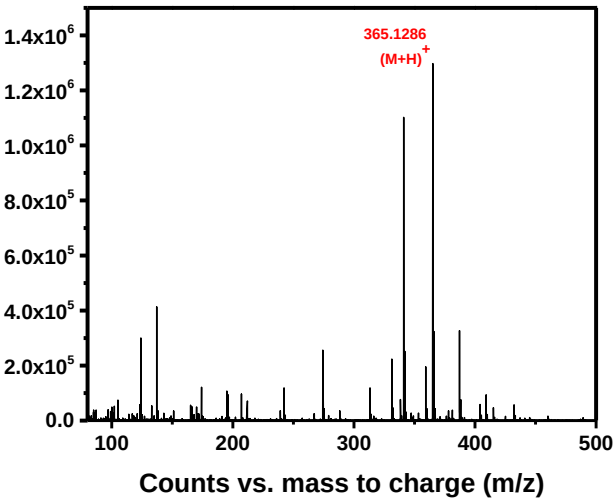



**Figure 5.25** HRMS spectrum of hnmh-$PLYH_2$. HRMS ($CH_3CN$, positive ionization): calcd. for $C_{63}H_{42}Fe_2N_6O_9$ m/z = 365.1290 $(M+H)^+$, found 365.1286 $[M + H]^+$.

…